Reaction Mechanism and Size-dependent Electrochemical Properties Study of $Cu_{2-x}S$ Versus Li

A Thesis

Presented to the Faculty of Graduate School

of Cornell University

In Partial Fulfillment of the Requirements for the Degree of

Master of Science

By Yuan Yao

August 2018

Abstract

$Cu_{2-x}S$ as one of the first tested battery anode material [1] has attracted a large amount of attention due to its high specific theoretical capacity (560 mAh g^{-1} for CuS and 337 mAh g^{-1} for Cu_2S) [2],

high energy density and good electronic conductivity for fast reaction kinetic (10^{-3} Ω^{-1} cm^{-1} to 140 Ω^{-1} cm^{-1} [3], [4]) . However, the reaction mechanism of $Cu_{2-x}S$ versus Li has not been elucidated. Also, as the technology advances, the $Cu_{2-x}S$ nanoparticle can be synthesized with great control over size, phase, and morphology. Whether nanostructuring will benefit the battery performance of $Cu_{2-x}S$ remains a question.

In this thesis, we studied the structural change of $Cu_{2-x}S$ (three different phase particles, anilite $Cu_{1.75}S$, roxbyite $Cu_{1.81}S$ and djurleite $Cu_{1.94}S$) during discharge versus the lithium foil. Several advanced characterization tools (X-ray diffractometer, high-resolution transmission electron microscope) and electrochemical testing (galvanostatic charge-discharge) are used to observe the structural and electrochemical behavior. As a result, we proposed a common reaction mechanism for $Cu_{2-x}S$ versus Li-ion.

Moreover, given the ability to synthesis $Cu_{2-x}S$ nanoparticle with excellent size, morphology and dispersity control [5], we studied the size-dependent electrochemical properties of $Cu_{2-x}S$. We found as the size of the particle decrease, the electrochemical curve resembles more like a supercapacitor. However, as the particle grows, it shows discharge plateau which is typical of battery material. With Electron Energy Loss Spectroscopy and X-ray Photoelectron Spectroscopy, we studied the electronic structure of the material which helps us to explain the size-dependent electrochemical behavior.

This work is dedicated to my family for supporting me

all the way and making me who I am

Acknowledge

First and foremost, I would like to acknowledge my adviser Prof. Richard Robinson for giving me the opportunity to work on this project and helping me throughout the project. His vision, intelligence, and hard-working has inspired and motivated me to work on my research project.

I would also like to acknowledge my thesis committee member, Prof. Jin Suntivich for the helpful discussions and guidance. His lectures on kinetic and diffusion have been of great assistance for conducting my research.

Thanks to Anuj Bhargava for mentoring me in the lab and for all the help with the synthesis, electrochemical testing, and TEM. Your help in every aspect of my research was imperative to the completion of this work. I would also like to acknowledge Michael Zachman for his help with the high-resolution TEM and EELS data acquisition and analysis. Moreover, I would like to thank Andrew, Curtis, and Doug for their help with the synthesis, optical measurement and other general questions I had in the lab.

This work made use of the Cornell Center for Materials Research (CCMR) Shared Facilities, which are supported through the NSF DMR-1149036.

Table of Contents

Table of Figure

Chapter 1: Introduction

Introduction to Copper Sulfide $Cu_{2-x}S$ Material

$Cu_{2-x}S$ Crystal Structure

Copper sulfide ($Cu_{2-x}S$) is the most complicated binary Cu chalcogenide system. Due to historical reason and the numerous phases available, the naming of copper sulfide has been somewhat confusing. Also, even with the same stoichiometries, the structural difference between the crystals can lead to completely different properties. For example, before the 1940s, people believed Cu_2S was dimorphous and existed in the orthorhombic and isometric modification. Below 110 °C, the phase is orthorhombic (low chalcocite). However, above 110 °C, the particle transform into hexagonal plus an isometric phase (high chalcocite) [6]. The binary Cu-S system exhibits a rich phase diagram [7], and there are eight dominate phases *Fig.1.*

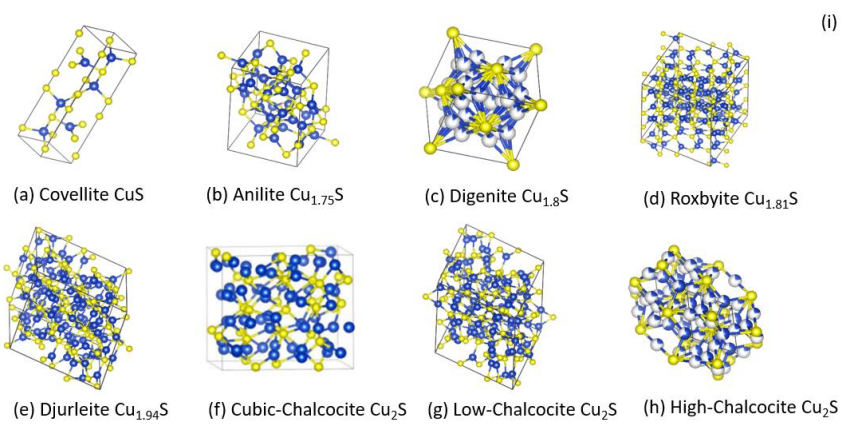

(i)

Name	Composition	Packing	Crystal system
Covellite	CuS	hcp	Hexagonal
Anilite	$Cu_{1.75}S$	fcc	Orthorhombic
Digenite	$Cu_{1.8}S$	fcc	Cubic
Roxbyite	$Cu_{1.81}S$	hcp	Triclinic
Djurleite	$Cu_{1.94}S$	hcp	Monoclinic
Cubic-Chalcocite	Cu_2S	fcc	Cubic
Low-chalcocite	Cu_2S	hcp	Monoclinic
High-chalcocite	Cu_2S	hcp	Hexagonal

Figure.1 (a) Covellite CuS (b) Anilite $Cu_{1.75}S$ (c) Digenite $Cu_{1.8}S$ (d) Roxbyite $Cu_{1.81}S$ (e) Djurleite $Cu_{1.94}S$ (f) Cubic-Chalcocite Cu_2S (g) Low-chalcocite Cu_2S (h) High-Chalcocite Cu_2S (i) Table of different $Cu_{2-x}S$ phases, structure, composition. [8]

The most common chalcocite phase is low-chalcocite which forms below 110 °C. The structure of low-chalcocite is determined to be monoclinic by Evan [8]. The distorted hexagonal framework consists of 12 sulfur atoms with 24 copper atoms sitting at the triangular interstices. In each unit cell, there are in total 48 S and 96 Cu [9]. High chalcocite structure is closely related to the low chalcocite structure and forms above 110 °C. Due to the high-temperature nature of this phase, the Cu atom is very mobile and makes identifying the exact atom position difficult. The copper atoms can occupy

tetrahedral, trigonal and linear coordination and the reported atomistic model is based on the statistical distribution of Cu atoms [10].

Djurleite ($Cu_{1.94-1.97}S$) is closely related to low chalcocite as they share the same monoclinic structure. Also, low chalcocite and djurleite always form together during synthesis [5], [11]. The unit cell of djurleite is composed of 62 Cu atoms with 52 atoms in the threefold, triangular coordination with S, nine are in tetrahedral sites and 1 in the linear coordination [11].

Roxbyite ($Cu_{1.81}S$) has a triclinic unit cell with 32 S atoms and 58 Cu atoms. Roxbyite is common in the nanocrystal synthesis [12], [13], [14], [15]. As reported by our group [16], roxbyite can transform into a copper-rich phase djurleite with the introduction of Zn ion into the system. As a result, the copper atom will be pushed into intrinsic Cu vacancy sites. However, the strain associated with this transformation will revert it into roxbyite phase.

According to the literature, anilite crystal has an orthorhombic structure. In the crystal, the sulfur atoms approximate a cubic face-centered arrangement and the copper atoms are ordered in the interstices [17]. Based on the first principle calculation, [12] anilite is one of the most stable forms of copper sulfide under Cu rich condition as it has the lowest heat of formation. Moreover, the XRD pattern of anilite can be easily differentiated from other $Cu_{2-x}S$ phases due to its unique single major peak at 46.5 degree.

X-ray Diffraction for $Cu_{2-x}S$

The complexity of the $Cu_{2-x}S$ phase diagram has made differentiating copper sulfide phases a nontrivial but necessary task. The most commonly used method is X-ray diffraction (XRD). Historically there is a debate about the differentiating the XRD pattern of chalcocite and djurleite. Looking at the XRD standard, we can find djurleite ($Cu_{1.94}S$), and chalcocite (Cu_2S) has very similar XRD patterns. Both

phases have three major peaks center around 38, 46 and 48 degrees in two-theta. Moreover, it is almost impossible to keep pure Cu_2S since the intrinsic instability of Cu_2S makes it quickly transforms to lower symmetry djurleite phase when exposed to air [10], [18], [19]. As such, a question about whether the XRD standard we used for chalcocite is correct was raised. After careful study of the XRD data, Burda *et al.* [20] first proposed a way to differentiate chalcocite and djurleite. The XRD pattern of djurleite ($Cu_{1.94}S$) has narrow peaks at 46.3 and 48.5 degrees. While chalcocite (Cu_2S) has peaked at 45.9, 48.5 degrees. Moreover, as pointed out by Lotfipour *et al.* [21] the subpeak at 26.2 and 55.7 degrees is unique to djurleite phase. The first pure Cu_2S nanocrystal was reported by Alivisatos group [22] under an inert atmosphere. Under transmission electron microscope, researchers from the Alivisatos group were able to observe the phases transformation between low-chalcocite (monoclinic) to high-chalcocite (hexagonal) which is induced by the electron beam irradiation. Moreover, after exposing to air, they observed a rapid phase transformation to djurleite phase.

Optical Measurement for $Cu_{2-x}S$

Another way to characterize different copper sulfide phases relies on the plasmonic behavior of $Cu_{2-x}S$ material [16], [23], [24]. It is well known that copper sulfide material has stoichiometry dependent vacancy concentration [25]. In non-stoichiometry $Cu_{2-x}S$ vacancies will form by loss of Cu to either oxygen or carbon dioxide at the free surface or a grain boundary [7], [25]. The vacancy concentration in $Cu_{2-x}S$ is generally understood to be stoichiometry dependent and increases with the number of Cu vacancies with reported carrier densities typically on the order of 10^{21} cm^{-3} [7]. Using UV-VIS near-infrared spectroscopy, we can measure the plasmonic peak centered around 1300nm. With careful control of the solution concentration. The intensity of the plasmon peak can be correlated back to the stoichiometry of the $Cu_{2-x}S$.

Oxidization State of $Cu_{2-x}S$

For a very long time, people believe for all $Cu_{2-x}S$ species the oxidization state of S remains as -2 while the Cu oxidization state changes between +1 to +2 depending on the stoichiometry. Several X-ray photoelectron spectroscopy (XPS) data point out both Cu (I) and Cu (II) are presenting in the particle [26], [27]. However, some study from the early time also indicates both S^{2-} and S_2^{2-} are both presenting in covellite material [28]. A recent paper from Liberato Manna has shed some new light on this debate [29]. Using XPS, superconducting quantum interference device (SQUID) and electron paramagnetic resonance (EPR), they proved for all $Cu_{2-x}S$ stoichiometries, the Cu valency remains as +1, and the sulfur valence state varies from S^{2-} to S_2^{2-}. In their experiment, the researchers started with $Cu_{1.1}S$ and gradually incorporate more Cu (I) into the crystal. As more copper adds into the system, the S-S covalent bonds progressively break and makes room for the incoming Cu ion. The proposed oxidization state change is also corroborated by EPR and SQUID measurement. The Cu^+ is diamagnetic. Throughout the reaction, they observed consistent diamagnetism in the sample. Moreover, based on XPS data, the copper 2p spectrum remain the same with different Cu:S ratio ($Cu_{1.1}S$, $Cu_{1.3}S$, $Cu_{1.5}S$, and Cu_2S). Another point worth mention is that the whole experiment was conducted in the glove box and it is crucial to the success of this experiment. $Cu_{2-x}S$ can be easily oxidized when exposed to air which leads to the formation of Cu^{2+}.

Electronic Structure of $Cu_{2-x}S$

The electronic structure of $Cu_{2-x}S$ has also been studied in detail. The top of the valence band is mainly contributed from the sulfur 3p orbital. Moreover, the bottom of the conduction band is composed of the Cu 4s and 4p orbitals [30], [31]. As for chalcocite (Cu_2S), each Cu atom gives out one 4s electron, and each S atom contributes six p electrons. As a result, the valence band is filled and behaves like a semiconductor, the band gap for chalcocite is 1.2 eV. As the Cu contents decrease, vacancies will be created in the valence band which affects the valency of the sulfur. Also, as the hole concentration

increase, the contribution of Cu-p orbital at the conduction band will gradually decrease. [32] Little experimental study about the electronic structure for each non-stoichiometric $Cu_{2-x}S$ phases has been conducted since identifying each phase is a nontrivial task. The electronic structure of $Cu_{2-x}S$ is mainly obtained through the computational model. Djurleite ($Cu_{1.94-1.97}S$) is a very similar crystal structure as low-chalcocite. The unit cell of djurleite has 62 Cu atoms and 32 S atoms. 52 of the copper atoms are in threefold, triangular coordination with S, nine are in tetrahedral coordination and 1 in linear coordination. Also, the band gap for djurleite is slightly elevated compares to chalcocite [8] Digenite ($Cu_{1.8}S$) can exist in cubic, rhombohedral and hexagonal depending on temperature. The band gap for digenite sits at 1.5 eV. [33] Roxbyite ($Cu_{1.81}S$) has a very complex crystal structure. The unit cell of roxbyite crystal consists of 32 S atoms and 58 Cu atoms, all having triangular coordination. [34] Anilite ($Cu_{1.75}S$) has an orthorhombic crystal structure, with S atoms, occupy the fcc lattice, and Cu atoms sit on the interstices. [57] Also, due to the weaker p-d hybridization, anilite has lower Fermi level. In covellite (CuS) structure, Cu atoms have two different environments, CuS_3 units sit between two layers of CuS_4 unit along the c-axis. The CuS_4 layers are connected by S-S layers. [35] Due to the high hole concentration, covellite CuS is an anisotropic p-type semiconductor. Moreover, CuS has the highest band gap (2.0 eV) in $Cu_{2-x}S$ family.

Copper Sulfide Synthesis

History of $Cu_{2-x}S$ Synthesis

Copper sulfide is the most extensively studied copper chalcogenide due to its promising properties. $Cu_{2-x}S$ is p-type semiconductor with 1.2 eV (Cu_2S) -2.0 eV (CuS) direct band gap [20]. Also, it is

environmentally friendly since it uses the nontoxic and earth-abundant material for the synthesis [34]. Moreover, the numerous non-stoichiometry phases enable people to tune the carrier density of $Cu_{2-x}S$ by changing the Cu to S ratio during the synthesis [36]. The carrier concentration tunability is unique compared to most of the noble metal nanocrystal [37].

Driven by the advantages shown above, in the past decade, a significant amount of progress has been achieved by controlling the phase, size, and morphology of $Cu_{2-x}S$ nanoparticle. A wide range of synthesis methods have been studied including hydrothermal [35], [36], [37], solvothermal [35], [41], [42], [43], [44] , solventless [45] synthesis and colloidal hot injection/heat-up methods [21], [22], [14], [46].

The early work of $Cu_{2-x}S$ synthesis used single precursor source Cu thiolates. Thermal decomposition of Cu thiolates releases both Cu and S which forms $Cu_{2-x}S$ [14], [45], [47], [48], [49], [50], [51], [52]. The thermal decomposition reaction is of great initial interest due to its simplicity also the elimination of any side reaction. In 2003, Krogel's group successfully synthesized Cu_2S through thermal decomposition of Cu-dodecylthiolate ($CuSC_{12}H_{25}$) [45], [49], [50]. The formed $Cu_{2-x}S$ has nanoplates morphology which tends to self-assemble into stacked platelets. A typical reaction yield is 10 to 20mg (10-20%). Later on, several group adopted Korgel's method [48], [53], [54]. With some modification of the experimental procedure, different $Cu_{2-x}S$ morphologies were obtained. For example, with different stirring speed and time during the precursor preparation, nanowires with length up to several microns were synthesized [48]. Also, shorter alkyl chain precursor results in the formation of 2D nanosheets while longer chain leads to the formation of nanoplates [53]. Another single precursor mechanism has been studied as well. For example, Cu-dithiocarbamate is used to synthesize nano barrels, quantum dots and nanowires [55], [56], [57].

Solution Based Methods

In recent years, most of the researches focused on colloidal solution-based synthesis. Typically, two separate precursors for copper and sulfur will be dissolved in organic solvent such as oleylamine (OLA). The most common copper precursors are CuCl and copper acetylacetonate. As for sulfur, elemental sulfur is normally used. For example, one of the recent $Cu_{2-x}S$ synthesis paper from our group [5] used CuCl and element S as precursors both of which are dissolved in a 7:3 oleylamine (OLA) octadecene (ODE) mixture. Solution-based synthesis can be separated into heat up method and hot injection. In heat up method, the two precursors are mixed at a low temperature and then heat up to the reaction temperature. One of the good examples of heat up method was from Wang's *et al.* publication. Using CuCl and S powder as precursors and OLA and TOPO solution as a solvent, they managed to grow monodisperse CuS nanoplates [58]. Moreover, they found changing the Cu to S ratio can directly change the plasmonic property of the CuS particle without changing the particle size and morphology.

To enable industrial application of $Cu_{2-x}S$ nanoparticle, a scalable, reliable synthesis need to be developed. With this mission in mind, researchers from Robinson's group developed a heat up method and obtained 30 grams of nanoparticle from a single batch synthesis [59]. After the initial success, they developed another super high concentration heat-up method and synthesized over 200g (80% yield) of nanoparticle from a single batch synthesis [5]. Also, even with large-scale synthesis, the 8nm roxbyite ($Cu_{1.81}S$) particle has a size dispersity less than 10%. In this synthesis, CuCl and S were used as precursors and 7:3 oleylamine (OLA) octadecene (ODE) mixture was used as a solvent. The CuCl and S are separately dissolved and mixed at 50°C which was followed by heating to 185°C for 2 hours. The products are then washed with acetone hexane mixture using the centrifuge three times. As described by the author, the key to this method is the high precursor concentration (1000 mM of CuCl 5000 mM of

S). The high concentration leads to the high viscosity of the solution which slows down the Ostwald ripening process. The retarded Ostwald ripening helps to reduce the size dispersity of the particle even after scaling the reaction up to 4 liters.

Apart from heat up method, another type of colloidal synthesis is the hot injection method. In that case sulfur precursor is typically injected into copper precursor solution under reaction temperature [46], [37], [59], [51]. Due to the high mixing temperature, hot injection reaction finishes a lot faster compare to heat up method. For example, Liu *et al.* [60] demonstrated a monodisperse $Cu_{2-x}S$ particle with a size between 2.8nm to 13.5nm can be synthesized through the hot injection method within 1.5 to 3 mins. The size variation was achieved by different injection temperature (115°C - 140°C). Moreover, they found that solvent choice has a strong influence on the phase of the synthesized $Cu_{2-x}S$ particle. Using OLA as solvent lead to djurleite ($Cu_{1.94}S$) and Oleic acid (OA) result in the formation of covellite (CuS) phase particle. Interesting, researchers also studied injecting copper precursor into S [25], [22], [46]. One of the highly cited paper was from the Alivisatos group in which they injected $Cu(acac)_2$ OA solution into DDT, ammonium diethyldithiocarbamate and OA mixture at 110°C. They successfully synthesis Cu_2S [22] particle and $Cu_{1.94}S$ [25]quantum dot through this method.

Hydrothermal Method

While typically used for the slowly growing large single crystalline particle, the hydrothermal method has been proven to be able to produce $Cu_{2-x}S$ nanocrystal with different morphologies. For example, Lu *et al.* reported successful synthesis of the $Cu_{2-x}S$ nanowire, nanotube and nanovesicle like structures using the hydrothermal synthesis method [38]. The 1-D structures are composed of self-assemblies of $Cu_{2-x}S$ nanoplates and nanoparticles. The ligand was found to determine the self-assemblies structure. For example, Triethylenediamine leads to the formation of the nanowire. Moreover, hydrothermal and solvothermal synthesis method has been proven to be very effective in

synthesizing $Cu_{2-x}S$ 3-D superstructures. For example, using copper nitrate, sulfur powder, and EG at 140 °C for 24 hours [61], a 3-D structure formed by four hexagonal CuS plates was synthesized. It has a diameter of 1-1.5 um and thickness of 200 nm. What is interesting about this structure is the 14 highly symmetric cavities which could enable possible application such as photocatalyst. Other hierarchical CuS structures such as flower-like structure and nanosphere have also been produced [62], [63].

Template Based Approach

Although self-assembly has been proven to be an effective way of building superstructure, the exact process is affected by various factors including capping ligand, reaction temperature, precursor. Also, it is very difficult to specifically design a self-assembly process which leads to the desired morphology. Templating gives researchers more control over the morphology of the particle and also promise better reproducibility. However, the size of the template is typically in the sub-micron range which limits the minimum size of the product [34]. Cu_2O crystal is only of the most common sacrificial template used for template-based $Cu_{2-x}S$ synthesis. For example, Jiao *et al.* demonstrated treating Cu_2O crystal with different initial geometry with Na_2S aqueous solutions can form anilite ($Cu_{1.75}S$) mesocages with cubic, octahedral and star-like morphology [64]. During the reaction, nano-Kirkendall effect leads to the formation of $Cu_{1.75}S$ on top of the Cu_2O skeleton. After removing the template with ammonia, a 3-D $Cu_{1.75}S$ superstructure is left behind.

Copper Sulfide for Battery Application

Mechanistic Study for $Cu_{2-x}S$ Lithium-Ion Battery

The battery as the primary energy storage device which bridges between sustainable energy sources such as solar power to the actual application has attracted a vast amount of attention in recent years. Among all the electrode materials, CuS is one of the first tested cathode material for lithium-ion batteries. It has several advantages including high specific capacity 561 mA.h/g, good electronic conductivity, relatively flat discharge curve and the use of low-cost abundant materials [3]. CuS reaction mechanism has been extensively studied before. Based on electrochemical data, the discharge curve of CuS can be separated into two regions. The first region is around 2.05 V and the second one is at 1.68 V [65], [66]. For the first region, two reactions mechanisms have been proposed. The first theory is that Li ions intercalate into the CuS structure and form Li_xCuS [65]. The reaction process can be described by the chemical equation below.

$$CuS + xLi^+ + xe^- = Li_xCuS$$

According to literature from Yamakawa *et al.* [67], using X-ray diffraction, they found the formation of Li intercalation compound Li_xCuS in the first region.

The second theory proposed that Li react with CuS and form Cu_2S intermediate phase and Li_2S [66].

$$CuS + xLi^+ + xe^- = (x/2)Li_2S + Cu_2S$$

Using *ex-situ* XRD and *in-situ* TEM, Tarascon *et al.* [66]found the formation of $Cu_{2-x}S$ nonstoichiometry phases as well as Cu_2S during the first discharge plateau.

The confusion is mainly caused by the complexity of $Cu_{2-x}S$ phase and the difficulty of identifying $Cu_{2-x}S$ material other than X-ray diffraction. Due to the similarity of XRD patterns, it would be difficult to differentiate a Li intercalation (d-spacing increase) from an actual phase transformation.

Other than the first region, the second region reaction mechanism has been identified to be displacement reaction. Typical metal chalcogenides such as Cobalt sulfide and Nickle sulfide undergo conversion reaction during discharge against Li. After the conversion reaction, the metallic particle will be sitting inside the Li_2S matrix. However, Tarascon's group [66] first observed that $Cu_{2-X}S$ follows a distinctive displacement reaction. During the reaction, copper ions are replaced by the incoming Li-ion with the anion lattice unmoved. As a result of the complete phase separation, Cu dendrites form on top of the Li_2S matrix. The displacement reaction instead of conversion reaction brought attention to several other research groups. Leveraging the powerful in-situ high-resolution TEM, Yi Cui *et al.* [68] managed to image the displacement reaction and present the dendrite growth through videos.

The reasons behind this unique feature of $Cu_{2-x}S$ are concluded in three points [68]. First, due to the high vacancy concentration and disordered structure, $Cu_{2-x}S$ has much higher ion diffusion coefficient compared to another metal chalcogenide ((D_{Cu} = 10−7−10−8 $cm^2 \cdot s^{-1}$ for low chalcocite at room temperature versus D_{Fe} = 10−17 $cm^2 \cdot s^{-1}$ for Fe_2S at 100 °C) [69], this enables the Cu to diffuse out of the initial lattice. The second reason is that Cu_2S and Li_2S has a very similar structure, this leads to minimum displacement of the S lattice during the reaction. Third, Cu in Cu_2S has a relatively low oxidization state of +1. Compare to the counterpart (Co_3S_4, FeS_2), it requires less amount of Li to react with per mole of material.

Capacity Retention

Despite all the advantages mentioned above, copper sulfide suffers from rapid capacity fading after the initial discharge cycle. The bad capacity retention is caused by the large volume changes during the displacement reaction. Also, most importantly, the dissolution of Li_2S into electrolyte after the first discharge reaction [68], [65]. Several approaches have been studied to alleviate this problem. In Chung's

et al. paper [65], they limit the voltage window to 2.6 to 1.8V and use ether-based electrolyte (LiTFSi dissolved in DME/DOL) to replace carbonate-based electrolyte. As a result, the capacity retention was over 70% after 60 cycles. Interestingly, a recent report [70] shows using Na rather than Li as the anode material, without the voltage window limitation but use ether-based electrolyte, they achieved extremely stable capacity retention over 400 cycles. Another way to improve the capacity retention is using conductive matrix typically carbon. Recent studies show carbon matrix can effectively capture polysulfide and prevent Li_2S dissolution [71]. Moreover, the conductive skeleton improves the conductivity of the whole electrode and also alleviate the volume change problem.

Another way to improve the electrochemical properties of $Cu_{2-x}S$ is by using novel nanostructured morphologies. For example, hollow spheres [72], nanowires [73], nanoflakes [74]. For example, ultrathin $Cu_{2-x}S$ nanosheet was tested for its electrochemical properties [75]. Due to the extremely high surface area. The first discharge cycle almost reached the theoretical capacity of 506 mA.h/g. Although, the capacity decrease to 321 mA.h/g at the 20^{th} cycle. Interesting, due to some surface activated process. The capacity increase to 642 mA.h/g at the 270^{th} cycle which is higher than theoretical capacity.

Chapter 2: Experiments and Results

Part 1: General Phase Transformation Path for $Cu_{2-x}S$ Polytypes Reacting with Lithium

Abstract

In this paper we study three different $Cu_{2-x}S$ polytype phases reaction with Li between the voltage range of 2.7 V to 1.8 V. Using *ex-situ* XRD and UV-Vis spectroscopy, we find regardless of the starting phases, the end products are always Cu_2S. Based on the XRD and UV-Vis result, we clarify the debate of Li and $Cu_{2-x}S$ first plateau reaction mechanism. Also, we propose a general reaction mechanism for all $Cu_{2-x}S$ polytype phases reaction with Li.

Introduction

To meet the industrial standards for applications such as electric vehicles and grid-scale energy storage, a significant amount of research has been devoted to exploring new electrode materials and to improve charge capacity and power.

$Cu_{2-x}S$ as one of the first tested battery anode material [1] has attracted large amount of attention due to its high specific theoretical capacity (560 mAh g^{-1} for CuS and 337 mAh g^{-1} for Cu_2S) [2] for high energy density and good electronic conductivity for fast reaction kinetic (10^{-3} Ω^{-1} cm^{-1} to 140 Ω^{-1} cm^{-1} [3][4]) .

Several *ex-situ* and *in-situ* XRD and TEM studies [1], [66], [68], [70] have been conducted to understand the $Cu_{2-x}S$ reaction mechanism. For CuS, two voltage plateaus are observed during the discharge. The first plateau occurs at 2.1 V and the second plateau at 1.7 V. As for Cu_2S, only one plateau is observed at 1.7 V. For the other $Cu_{2-x}S$ polytypes, the same two plateaus behavior as CuS are observed but with a shorter first plateau.

The reaction occurring at the second discharge plateau (1.7 V) is generally agreed to be a displacement reaction [66], [68]. During displacement reaction, Li ions replace Cu ions in the $Cu_{2-x}S$ lattice

with the sulfur anion lattice intact. As for the first plateau, the mechanism is still under debate. Some researches found it is a Li intercalation reaction and the mechanism can be described by the equation below [65], [67].

$$CuS + Li^+ + e^- = LiCuS$$

However, others believe during the first plateau, CuS transform to Cu_2S as an intermediate phase and it is demonstrated by the equation below [1], [66].

$$2CuS + 2Li^+ + 2e^- = Li_2S + Cu_2S$$

This paper aims to resolve the debate and find a general first lithiation plateau reaction mechanism for numerous $Cu_{2-x}S$ polytypes.

Results

Three different phases $Cu_{2-x}S$ bulk particles are used in this study, the high chalcocite (Cu_2S) and roxbyite ($Cu_{1.81}S$) particle are synthesized by modifying the high concentration $Cu_{2-x}S$ method reported from our group [5] (varied Cu and S precursor ratio and concentration). The anilite ($Cu_{1.75}S$) particle is purchased from Fisher Scientific. All particle and solvent are used as received without further purification. Coin cell set up is used for all electrochemical experiment. Electrodes are made through doctor blading on the carbon substrate. Lithium foil is used as the anode. Bruker D8 X-ray diffractometer paired with a Hi-STAR area detector is used for X-ray diffraction measurement. Cary 5000 UV-Vis-NIR spectroscopy is used for all-optical measurement with tetrachloroethylene as a solvent. As for high-resolution TEM, FEI Titan Themis CryoS/TEM was used with accelerating voltage of 300kV. Other experimental details are provided in SI.

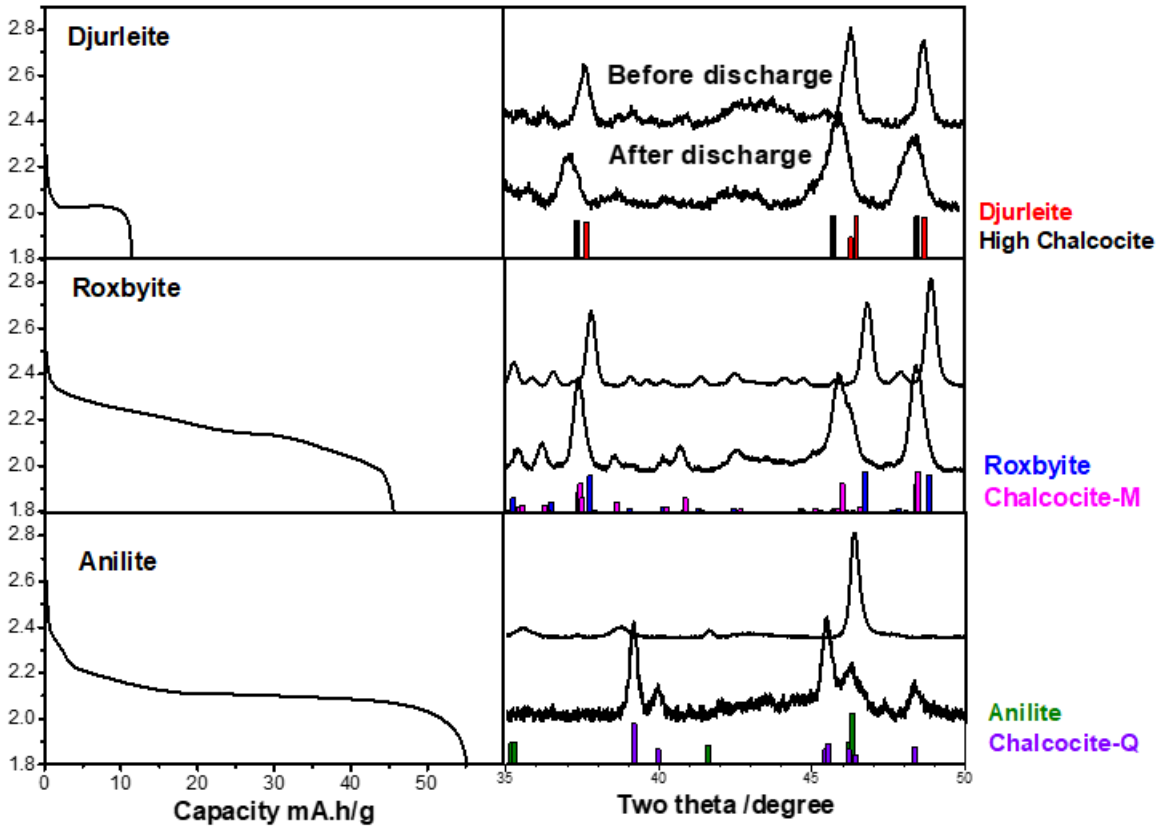

*Figure. 2 (a-c) Galvanostatic discharging of (a) Djurleite, (b) Roxbyite, and (**c**) Anilite at C/20 rate in the voltage range of 2.7 V to 1.8 V. (**d-f**) Corresponding XRD pattern before and after discharge (**d**) ex-situ XRD pattern for Djurleite (**e**) XRD pattern for (**f**) ex-situ XRD pattern for Anilite.*

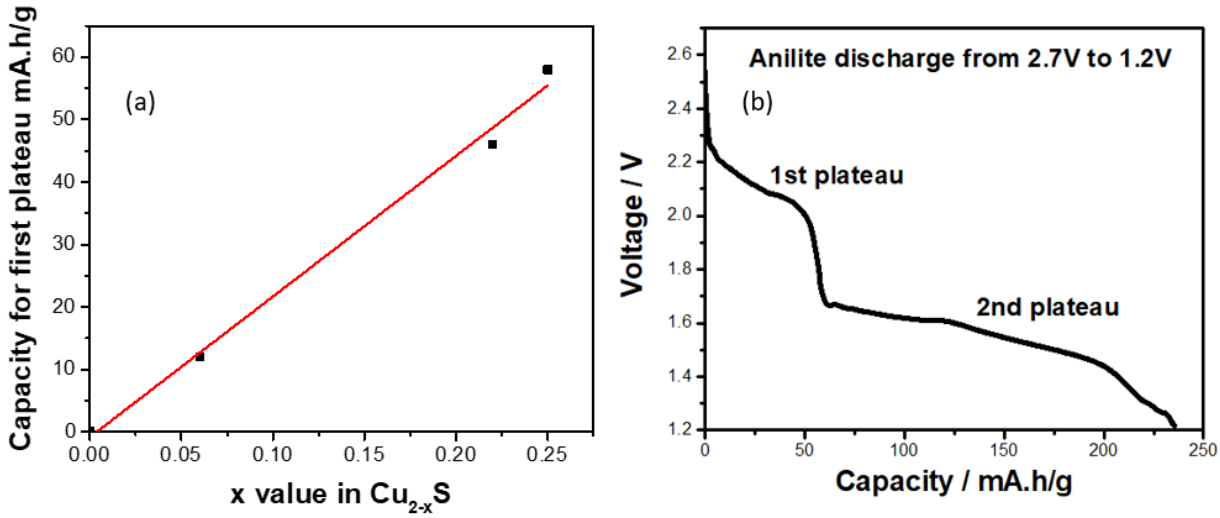

Figure. 3 (a) First plateau capacity of the Cu2-xS phases versus the corresponding x value. (b) Full discharge profile of Anilite particle from 2.7V to 1.2V

To investigate the reaction mechanism of $Cu_{2-x}S$ with lithium, three bulk $Cu_{2-x}S$ polymorphs, djurleite ($Cu_{1..94}S$), roxbyite ($Cu_{1.81}S$), and anilite ($Cu_{1.75}S$) are discharged through the 1st plateau (2.7 V to 1.8 V) and the corresponding *ex-situ* XRD pattern was measured at the beginning and end of the voltage range. In general, a full discharge curve (2.7 V to 1.2 V) of $Cu_{2-x}S$ has two plateaus. The first plateau sits at 2.1V and the second one sits at 1.7V. (**Fig. 3(b)** shows the full discharge profile for the anilite ($Cu_{1.75}S$)). As mention in the introduction, we are interested in understanding the reaction mechanism of the first plateau. As such, we only discharge all the materials between 2.7 to 1.8 V. As we can see from the 1st plateau discharge profiles for djurleite ($Cu_{1..94}S$), roxbyite ($Cu_{1.81}S$), and anilite ($Cu_{1.75}S$) (**Fig. 2(a) – (c)**), the capacity from the first plateau is lowest in the djurleite ($Cu_{1.94}S$) sample 11 mA.h/g and highest in the anilite ($Cu_{1.75}S$) sample 56 mA.h/g. To study the relationship between $Cu_{2-x}S$ stoichiometry and the first plateau capacity, we plot the x value in $Cu_{2-x}S$ versus the capacity from the first plateau (**Fig. 3(a)**). A linear relationship is observed between the discharge capacity and the Cu stoichiometry. The linear relationship between capacity and stoichiometry is expected for a phases transformation between $Cu_{2-x}S$ to Cu_2S. Since the amount of Li can react with the material is determined by the value x. However, for the Li intercalation reaction, the amount of Li ions can intercalate into the material is determined by how much lattice strain the lattice can withstand. It is unlikely to follow a linear relationship.

The XRD patterns show three distinct initial phases, but patterns for the final phases show very similar structures. The three initial XRD pattern for the electrodes match the reference peaks expected for djurleite ($Cu_{1.94}S$), roxbyite ($Cu_{1.81}S$), and anilite ($Cu_{1.75}S$) **Fig. 2(d), (e), (f)**, respectively. Also, **Fig. 9** shows XRD pattern for as synthesis materials). At the end of the first plateau (1.8 V), the three samples have shifted peak positions to positions that likely correspond to a Cu_2S phase.

For the djurleite ($Cu_{1.94}S$), the main peaks at 2θ of 37.6°, 46.5° and 48.8° shift to 37.2°, 45.8° and 48.3°, respectively (**Fig. 2d**). The positions of the 45.8° and 48.3° peaks align well with the high chalcocite (Cu_2S) phase. From these close alignments, we conclude the phase has transformed to high chalcocite

(Cu_2S). The 37.2 ° peak position, while not aligning precisely with the high chalcocite (Cu_2S) phase (37.4 °), is shifted from the initial 37.6 ° by 0.4 °, which could indicate a strain of 1.2% from the initial djurleite ($Cu_{1.94}S$) plane (8 0 4) or a strain of 0.7% from the high chalcocite (Cu_2S) plane (1 0 2). Scherrer broadening analysis gives values of 29.6 nm and 15.1 nm as the initial (2.7 V) and final (1.8 V) grain size. (detail Shown in **Fig. 12, Tab. 3**) XRD results show during the discharge, the initial djurleite ($Cu_{1.94}S$) phase transform to high chalcocite (Cu_2S) phase with significant particle size decrease.

For roxbyite ($Cu_{1.81}S$), the major peaks of 37.6 °, 46.5 ° and 48.8 ° shift to 37.1 °, 45.8 °, and 48.3 °, respectively (**Fig. 2e**). Before discharge, all three major peaks along with the minor peaks agree well with the roxbyite ($Cu_{1.81}S$) standard. After discharge, the three main peaks shift to positions that perfectly match the chalcocite-M (Cu_2S) standard. Also, several sub-peaks emerge (40.7 °, 36.3 °) which are unique to the chalcocite-M (Cu_2S) phase. Based on the Scherrer broadening analysis, the average particle size decreases from 30.4nm to 18.17nm. Overall, the *ex-situ* experiment indicates a similar effect as djurleite ($Cu_{1.94}S$) except the end phase is chalcocite-M (Cu_2S) instead of high chalcocite (Cu_2S). These two phases are closely related as chalcocite-M is the low-temperature stable structure and high chalcocite become stable at the temperature above 103.5 °C. Crystallographically, chalcocite-M and high chalcocite phases both have hexagonal superlattice (slight distortion) but with different Cu arrangement[34].

For anilite ($Cu_{1.75}S$), after the discharge to 1.7 V, the main peak at 46.4 ° significantly decreases in intensity, and new peaks emerge at 39.2 °, 39.95 °, 45.45 ° and 48.3 ° (**Fig. 2f).** The XRD pattern of the sample at 1.7 V agrees well with the chalcocite-Q (Cu_2S) standard. Based on Scherrer broadening analysis, the particle size decreases from 29.7nm to 22.9nm.

In all three discharge experiments, we observed a phase transformation to Cu_2S phases along with a 25% to 50% particle size decrease. The *ex-situ* results agree well with Tarascon [66] previous study in which he observed the formation of Cu_2S and Li_2S near the end of the first discharge plateau for CuS.

Moreover, a clear phase contrast was observed in his HRTEM image which indicates it is a phase transformation rather than Li intercalation. In our case, The only potential lattice expansion was observed in the djurleite ($Cu_{1.94}S$) particle for one peak.

The particle size decrease has been observed in $Cu_{2-x}S$ and other battery materials [10], [11]. It is attributed to the volume change during phase transformation or Li intercalation [78], [79]. Moreover, in this case, as Li_2S form inside the active material and dissolves into electrolyte [65], [68], the disintegration process is accelerated compares to other materials such as silicon.

Overall, since for all three compositions the only end product of the first plateau reaction is Cu_2S and little evidence supporting the Li intercalation mechanism was found, we conclude that the reaction mechanism of the first plateau is phase transformation rather than Li intercalation.

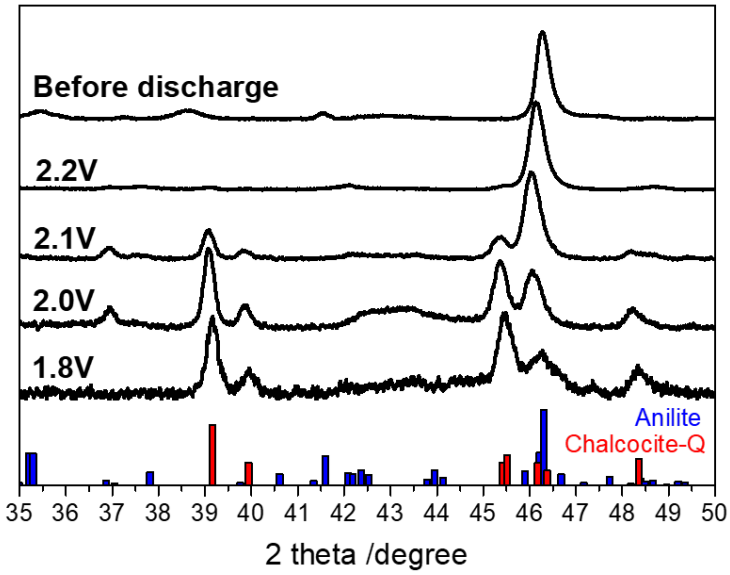

Figure. 4 (a) Ex-situ XRD for anilite particle discharge to four different voltages (2.2V), (2.1V), (2.0V), (1.8V), anilite and Chalcocite-Q standard provide on the bottom. The initial anilite gradually transforms to Chalcocite-Q phase.

To understand the correlation between phase and the amount of Li reacted, we apply different potentials to the anilite (Cu1.75S) (as a model system) and record the corresponding XRD patterns. Four sets of anilite (Cu1.75S) particles are discharged to 2.2 V, 2.1 V, 2.0 V, and 1.8 V (Fig. 3). At 2.2V, the 46.4° peak shifts 0.1° to the left which can be translated into 0.2% lattice strain. After the initial peak shift, the main peak at 46.4 ° gradually decreases in intensity. Also, four new peaks appear at 39.1 ° (1 0 4), 39.95 ° (1 1 3), 45.45 ° (1 1 4) and 48.3 ° (2 0 2) which are aligned with chalcocite-Q. The good agreement between XRD data and standards indicates a phase transformation from anilite (Cu1.75S) to chalcocite-Q (Cu_2S) phase.

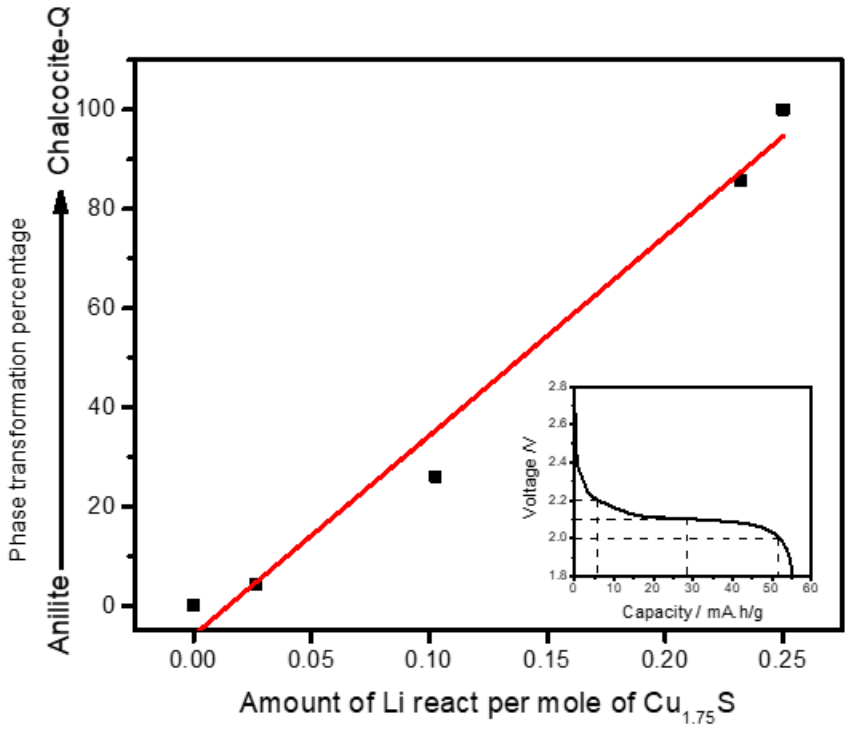

Figure. 5 Specific capacity plotted as a function of percentage phase transformation between anilite and high chalcocite. (inset) Corresponding capacity for the four different discharge voltages.

We correlate the amount of Li-ion reacted to the amount of phases transformation by examining the ratio of the XRD peak intensities for the anilite samples. For endpoints, we use the initial anilite ($Cu_{1.75}S$)

and the final, 1.8 V sample as the standard for a complete transformation to chalcocite-Q (Cu_2S). By taking the ratio of the peak at 45.45 ° and 48.3 ° (the major peaks of the two phases) we can quantify the phase transformation percentage (see **SI**). The discharge capacity is used as a measure of the amount of Li-ion reacting with the particle (**Fig. 5** inset shows the conversion of discharge voltage to capacity). The relationship between phase and specific capacity follows a mostly linear trend (**Fig. 5**). Based on these results, we propose a common reaction mechanism for the first discharge plateau between $Cu_{2-x}S$ and Li.

$$Cu_{2-x}S + xLi^+ + xe^- = (x/2)Li_2S + (1 - x/2)Cu_2S$$

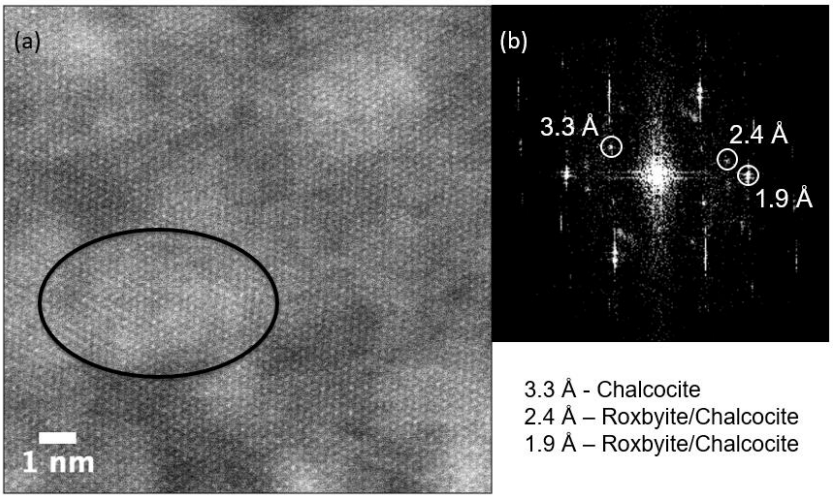

Figure. 6 High-resolution TEM was used to analysis the lithiated roxbyite particles. (a) Large flat roxbyite particles have an atomic lattice visible perpendicular to the supporting film (b) The corresponding Fast Fourier transformation image indicates the appearance of Chalcocite and roxbyite phases.

To get more detailed atomic information of the phases, high-resolution transmission electron microscopy (HRTEM) characterization is conducted on roxbyite ($Cu_{1.81}S$) particles after discharge to 1.9 V (in the middle of the first plateau reaction). The TEM images of the flat disk particles show an atomic lattice planes perpendicular to the supporting film (**Fig. 6a**, and also **Fig. 11**). Using fast Fourier transformation (FFT), three sets of lattice spacings are found In **Fig. 6b**. 0.19 nm corresponds to (0 16 0) plane for roxbyite ($Cu_{1.81}S$) phase, and 0.24 nm and 0.33nm corresponds to (1 0 2) and (1 0 4) planes for

high chalcocite (Cu_2S) phase (fitting standards in **SI Fig. 12**). Roxbyite was found to present in the whole field of view. However, spacing corresponding to chalcocite-Q phase was only found in the black circle. (**Fig. 6(a)**) The TEM images suggest that after discharge to 1.9V, the particles undergo a partial phase transformed from roxbyite ($Cu_{1.81}S$) to chalcocite-M (Cu_2S) phase which is consistent with the *ex-situ* XRD experiment shown in **Fig. 2**.

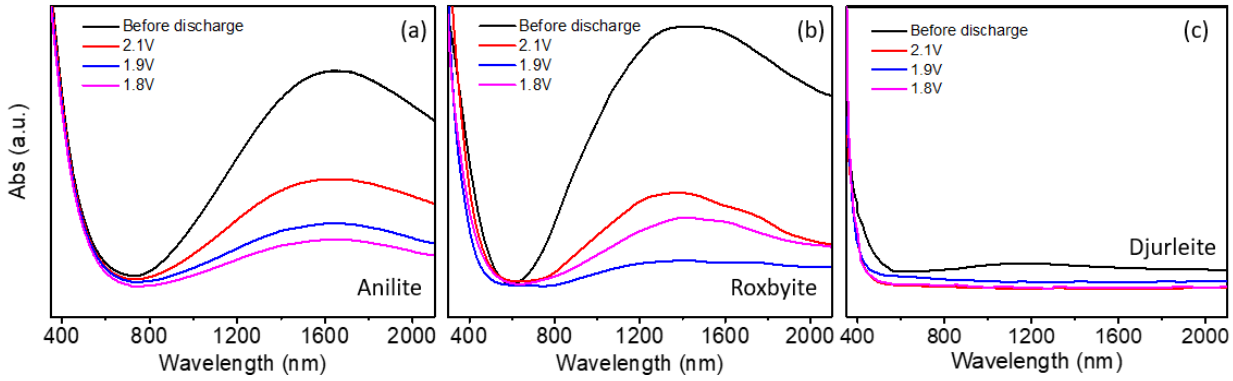

Figure. 7 Uv-vis (NIR) absorption spectrum for three different Cu2-xS phases crystal at four different discharge states. ***(a)*** *Anilite nanoparticle before discharge and discharge to 2.1V, 1.9V and 1.8V.* ***(b)*** *Roxbyite nanoparticle before discharge and discharge to 2.1V, 1.9V and 1.8V.* ***(c)*** *Djurleite nanoparticle before discharge and discharge to 2.1V, 1.9V and 1.8V.*

Another means to qualify and quantify a phase transformation between the $Cu_{2-x}S$ phases is by characterizing the localized surface plasmon resonance (LSPR), which is dependent on the excess charge (vacancy) concentration and thus the stoichiometry [11], [12]. As the x value increase in $Cu_{2-x}S$, the vacancy concentration will increase, resulting in a more intense LSPR peak and with a blue shift [31]. We characterized the LSPR for the three different phase particles, djurleite ($Cu_{1..94}S$), roxbyite ($Cu_{1.81}S$), and anilite ($Cu_{1.75}S$), during discharge by *ex-situ* Uv-vis (NIR) spectroscopy. Close examination of the UV-vis (NIR) absorption spectra of all three $Cu_{2-x}S$ samples at four different discharge states (**Fig. 7**) provides additional evidence for the phase transformation mechanism. As shown in **Fig**. **7a, b**, for anilite ($Cu_{1.75}S$) and roxbyite ($Cu_{1.81}S$) the LSPR decreases significantly after the discharge, which indicates the number of free charge carriers decreases, likely due to a transformation towards a more copper-rich phase (Cu_2S).

For the djurleite ($Cu_{1.94}S$) phase, only a small plasmon peak was observed before discharge because the stoichiometry of djurleite ($Cu_{1.94}S$) has few free vacancies (it is very close to the end product Cu_2S). However, after discharge to 1.9V, the small plasmon peak disappears, which indicates the particle transform to perfect Cu_2S phase. Based on the procedure developed by Luther *et al.*, we calculate the carrier concentration based on our absorbance measurements [24], [25]. The results are present in **Fig. 8**. (For Djurleite, the Full-Width Half Max was only measurable for the original sample).

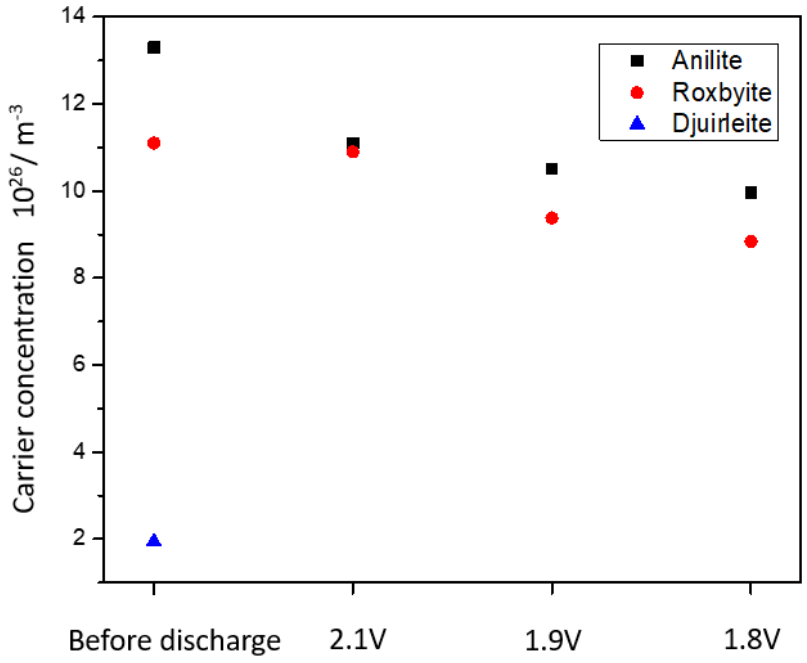

Figure. 8 Carrier concentration evolution for three phases material. Calculation base on optical measurement. (Only one point was measurable for djurleite phase)

The calculated carrier concentration is in the right range compare to the reported value for $Cu_{2-x}S$ [25], [37]. For both anilite and roxbyite, as the applied potential decrease, the carrier concentrations gradually decrease which indicate the particle is reacting toward Cu_2S. Comparing in between phases, Anilite always has the highest carrier concentration, and djurleite is the lowest. The optical data is also consistent with our expectation that the closer to Cu_2S, the less charge carrier will present in the particle. Overall, based

on the optical and XRD data, we can conclude that after the first plateau at 2.1 V, the initial $Cu_{2-x}S$ phases always transform to Cu_2S phase.

Future work

Introduce $Cu_{2-x}S$ with lower Cu content (CuS) for added proof

Adding phases such as covellite (CuS) and conduct the same ex-situ XRD experiment. If the final phase is still chalcocite (Cu_2S), we can study whether the phase transformation process has intermediate phases (roxbyite or digenite). If the final phase is not chalcocite (Cu_2S) then we can study why is there a phase dependence on the Li – $Cu_{2-x}S$ reaction mechanism.

In-situ TEM study during the lithiation process

During our experiment, we did not observe the phase transformation process. Conducting a high-resolution *in-situ* TEM experiment will help us to understand how the phase transformation process in more detail. For example, it reveals any intermediate phase during the reaction.

Studying the lithiation process under fast discharge (kinetically limited)

The phase transformation from $Cu_{2-x}S$ to Cu_2S requires structural rearrangement. However, this reaction might become diffusion limited when we increase the discharge rate. If the phase transformation is no longer the preferential reaction mechanism at a faster discharge, we can study the kinetically limited reaction mechanism. And also, finding the crossover point for the two mechanisms.

Conclusion

Using X-ray diffraction, high-resolution TEM, and UV-vis spectroscopy, we studied the first discharge plateau of $Cu_{2-x}S$ versus Li. Regardless of the starting phases, we found after the first discharge

plateau, all three phases transform to Cu_2S phase. All the data suggests a common reaction mechanism for the large variety of $Cu_{2-x}S$ polytype phases.

Supporting Information

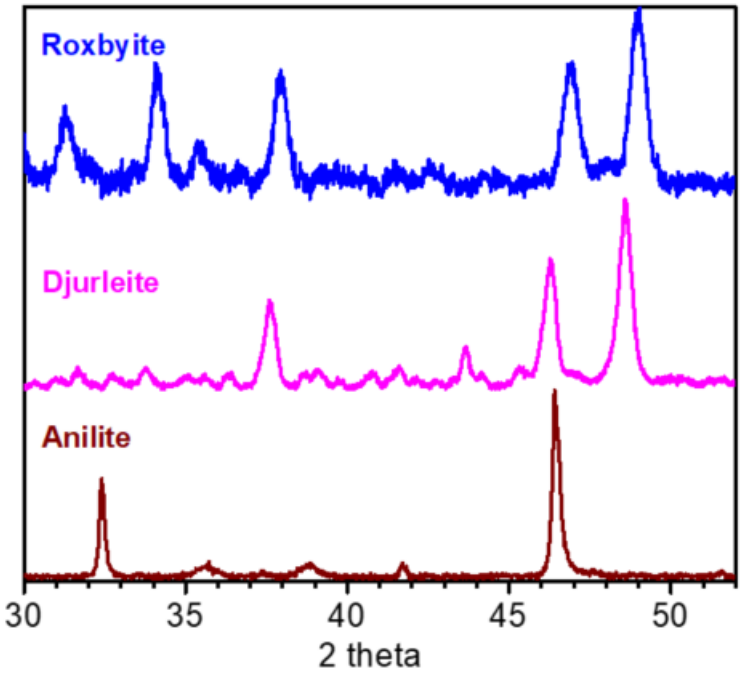

Figure. 9 XRD plot of as-synthesized phases of Copper Sulfide

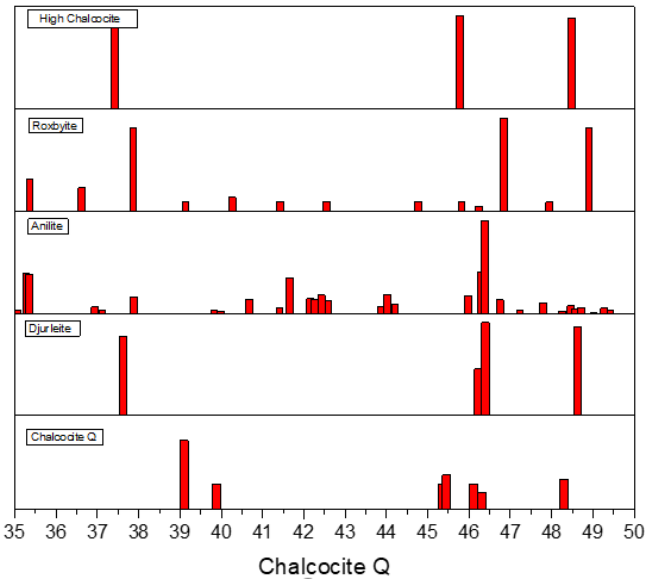

Figure. 10 XRD standard used for fitting the ex-situ XRD data

Table. 1 The X-ray diffraction standard and their corresponding PDF card number

PDF#00-026-1116	PDF#00-029-0578	PDF#00-023-0958	PDF#00-023-0959	PDF#01-072-0617
High chalcocite	Chalcocite-Q	Roxbyite	Djurleite	Anilite

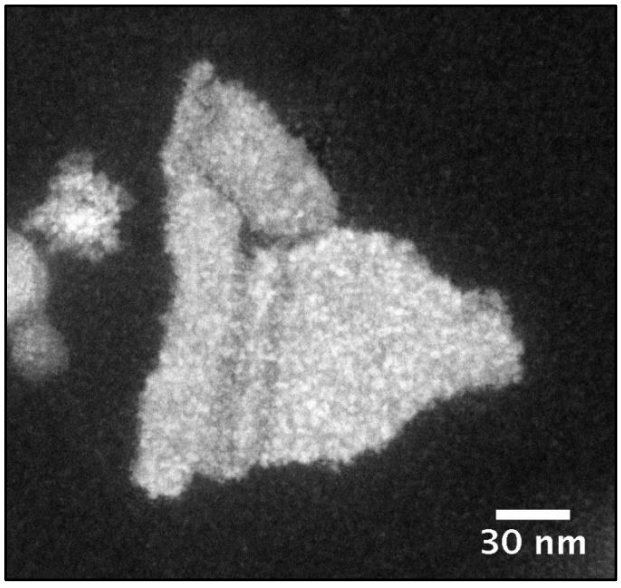

Figure. 11 Roxbyite particle prepared for HRTEM experiment

Table. 12 The fitting standard for all possible phases after lithiation, circle red for d-spacing close to 0.19 nm, blue circle for d-spacing close 0.23 nm

Roxbyite

2-Theta	d(Å)	I(f)
36.619	2.452	25
36.619	2.452	25
37.867	2.374	90
39.134	2.300	10
39.134	2.300	10
40.265	2.238	15
40.265	2.238	15
41.424	2.178	10
41.424	2.178	10
42.549	2.123	10
44.763	2.023	10
45.814	1.979	10
46.840	1.938	100
46.840	1.938	100
47.942	1.896	10
47.942	1.896	10
48.902	1.861	90

Li_2S

2-Theta	d(Å)	I(f)
26.981	3.302	100
31.241	2.861	20
44.781	2.022	40
53.061	1.725	23

Chalcocite-M

2-Theta	d(nm)	I(f)
36.233	2.480	18
37.322	2.410	50
37.393	2.400	70
37.448	2.400	35
38.605	2.330	25
40.182	2.240	13
40.803	2.210	35
45.922	1.970	70
46.502	1.950	13
48.346	1.880	70

Digenite

2-Theta	d(Å)	I(f)
35.907	2.499	12
37.248	2.412	12
40.078	2.248	23
46.299	1.959	100

High Chalcocite

2-Theta	d(Å)	I(f)
26.498	3.361	5
29.209	3.055	9
37.425	2.401	88
45.777	1.9805	100
48.488	1.8759	98
53.672	1.7063	45

Djurleite

2-Theta	d(Å)	I(f)
35.009	2.561	14
35.612	2.519	16
36.282	2.474	12
37.620	2.389	85
44.210	2.047	10
46.134	1.966	40
46.309	1.959	95
48.651	1.870	100

Table.3 Result of the Scherrer analysis for three different phases before and after discharge

	Before discharge		After discharge	
Full width half max (Radius)	46.15 degree peak	48.6 degree peak	46.15 degree peak	48.6 degree peak
Djurleite($Cu_{1.94}S$)	0.41	0.366	0.82	0.76
	46.58 degree peak	48.98 degree peak	46.58 degree peak	48.98 degree peak
Roxbyite($Cu_{1.81}S$)	0.377	0.38	0.81	0.525
	46.4 degree peak		46.4 degree peak	
Anilite ($Cu_{1.75}S$)	0.377		0.49	

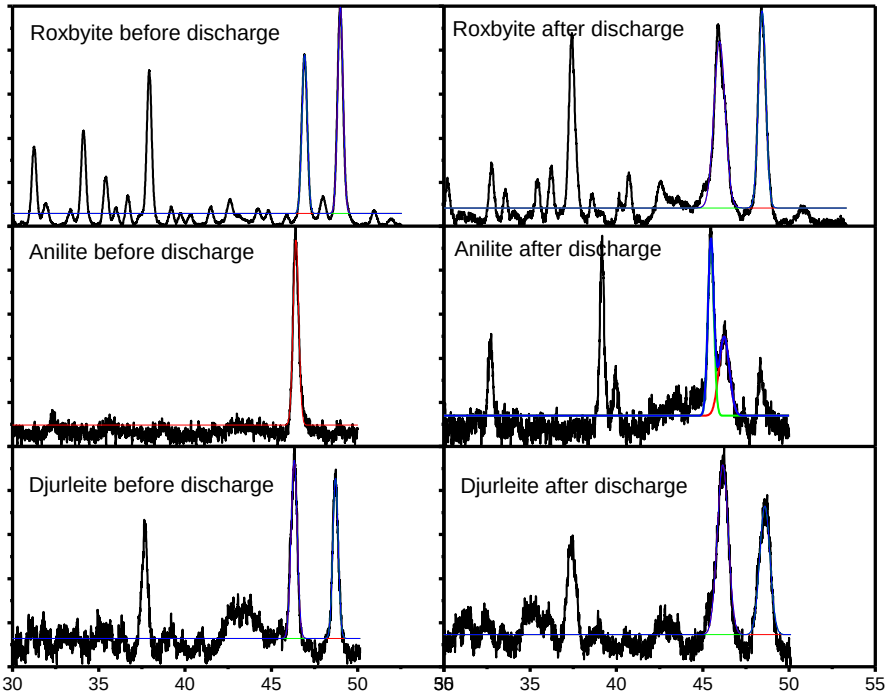

Figure. 12 Scherrer analysis of three different phases Cu2-xS before and after discharge

Calculating Percentage Phase Transformation

First, we assume at 1.8V, all the anilite transformed into Chalcocite-Q phase. We measured the peak intensity of the two characteristic peaks at 46.4 ° and 45.45 °. Using the peak ratio from 1.8V, we back calculated how much anilite are transformed into chalcocite-Q phase. For example, the ratio of 45.45 ° and 46.4 ° peak is 1 to 0.576. Moreover, the peak intensity from the 2.2V sample is 0.075 to 0.9448. We know the 45.45 ° peak only belongs to chalcocite-Q phase. Then the amount of anilite in the 46.4 ° peak can be calculated as

(0.9448-0.075*0.576)/0.9448=95.6%

Moreover, the amount of chalcocite-Q is 1-95.6%=4.4%

Using this method, we obtained ***Fig 5.(b)***

Part 2: Size-dependence of Li-mediated Phase Transformation in Roxbyite Nanodisks

Abstract

In this work, we study the size-dependent roxbyite nanodisks reaction with lithium and the corresponding reaction mechanisms. Instead of focusing on the well know displacement reaction for $Cu_{2-x}S$ (at 1.7 V versus Li), we study the reaction taking place at 2.1 V versus Li. Based on the electrochemical evidence from four different sizes (9.9 nm to 26.9 nm) roxbyite nanodisks, the plateau length is correlated to the particle size. Based on data from high-resolution transmission electron microscope and x-ray diffraction, the roxbyite nanodisks are found to transform to high chalcocite phase. Also, the lithium ions are found to intercalate preferentially through the side rather than the top face of the nanodisks. Furthermore, electron energy loss spectroscopy and x-ray photoelectron spectroscopy were employed to study the origin of the size dependence behavior. Smaller particles are found to have more Cu^{2+} present which could explain the size-dependent electrochemical properties.

Introduction

Current battery technology is limited regarding energy density and power density. To support the application such as an electric vehicle, significant research has been devoted to exploring new electrode materials and to improve the existing material with novel ideas such as nano-structuring and 3-D printing.

$Cu_{2-x}S$ is one of the most studied electrode material due to high theoretical specific capacity (560 mAh g^{-1} for CuS and 337 mAh g^{-1} for Cu_2S) [2] for high energy density and good electronic conductivity for fast reaction kinetic (10^{-3} Ω^{-1} cm^{-1} to 140 Ω^{-1} cm^{-1} [3], [4]). Moreover, it has a distinctive reaction mechanism compared to the other metal chalcogenides. Several studies [68], [66], [70] have pointed out that instead of the common conversion mechanism for metal chalcogenide, at 1.7 V versus Li, $Cu_{2-x}S$ materials react with Li-ion through displacement reaction. During the displacement reaction, the anionic lattice is fixed with only the Cu ion replaced by Li-ion. The displacement reaction happens mainly due to the structural similarity between Cu_2S and Li_2S and fast copper ion diffusion rate [68]. Despite all these promising properties, $Cu_{2-x}S$ materials have suffered from poor recyclability mainly due to the Li_2S dissolving in the electrolyte [65] and also Cu dendrite formation during the displacement reaction leading to internal shorting of the battery [68].

Detailed studies [1], [66], [68], [70] have been conducted to understand the $Cu_{2-x}S$ and lithium reaction mechanism. In general, two discharge plateaus are observed. The first plateau occurs at 2.1 V and the second plateau at 1.7 V. The reaction mechanism for the second plateau has been confirmed to be displacement reaction [66], [68] as discussed above. However, little attention has been paid to the first plateau. As such, we plan to explore the potential of the first plateau in this paper.

On the other hand, in recent years, nano-structuring has been proven to be a very effective method for improving material properties [80], [81], [82], [83]. For example, size-dependent extrinsic pseudocapacitor behavior was observed in several materials such as V_2O_5 [84] and $LiCoO_2$ [85], [86]. Taking $LiCoO_2$ as an example, as the particle size decrease from bulk to 6 nm, the typical well-defined discharge plateau gradually transforms to a sloped discharge curve which resembles the signature of supercapacitors.

The extrinsic pseudocapacitor behavior can be caused both due to thermodynamic and kinetic reasons. Kinetically, as the particle size decreases, the lithium ion diffusion path decreases, and the discharge process is no longer diffusion limited [87]. Thermodynamically, the discharge voltage plateau exists due to the specific Li site energy (amount of energy need for Li-ion to react) for each material. Due to the difference in the chemical environment, surface atom (top few nanometers) normally have different Li site energy as compared to the core of the material [86]. If the particles are large as compared to the thickness of the surface layer, the typical discharge plateau is expected. However, as the particle size decrease, surface atoms become a significant portion of the particles which leads to the sloped discharge curve instead of a plateau in the galvanostatic curves.

In this paper, four different sized roxbyite particles with sample hexagonal disk morphology were synthesized. Electrochemical discharge curves for just the first plateau showed a similar size dependent crossover behavior compare to $LiCoO_2$. To elucidate the mechanism behind this phenomenon, *ex-situ* XRD experiments are conducted for all four sized particles. The results showed roxbyite particles transform to Cu_2S phase after the first plateau and additionally, Li ions preferentially intercalate through the side of the nanodisk. Furthermore, electron energy loss spectroscopy and X-ray photoelectron spectroscopy are employed to study the fundamental reason for the size dependence.

Experiment

All the electrochemical testing, optical measurement, high-resolution TEM and ex-situ XRD experimental procedures are identical to Part I.

Synthesis

All the roxbyite particles are synthesized using high concentration method based on a previous paper published in our group [5] with 160 ^{o}C used as soaking temperature instead of 185 ^{o}C. Variation of the particle sizes is achieved by varying the Cu to S ratio during the synthesis (**Table. 4**).

Table. 4 Copper Ion to S Ratio Versus Particle Size

Cu:S mole ratio	2:1	2:1.3	2:1.5	2:1.55
Particle size	10nm	12.5nm	18nm	27nm

Dark Field Image and Electron Diffraction

Darkfield imaging is used to index the hexagonal particle. At first, an evaporating Al coated sample is scanned with the same setting for calibration. Then, the sample is sent into TEM, and normal imaging mode is used to find an area with a large number of particles. Then the TEM is switched to diffraction mode, and then the brightest spot is selected. After that, imaging mode is turned on again. As we can see, the bright surface corresponds to the diffraction spot we selected. FEI-F20 TEM is used for this experiment.

Electron Energy Loss Spectroscopy (EELS)

FEI Titan Themis CryoS/TEM 60-300 kV combine with an ultra-boost detector are used for EELS data collection. The 27 nm roxbyite particle is used for this experiment since we want to capture the EELS line spectra over a long enough distance for a single particle.

X-ray Photoelectron Spectroscopy (XPS)

XPS is conducted using Surface-science-instruments-SSX-100-XPS. The sample is retrieved from electrodes using the method previously described. Moreover, then, the particle is dissolved in hexane

and then drop cast onto a clean silicon wafer for XPS measurement. After the experiment, the data is processed by CASA-XPS.

Results and Discussion

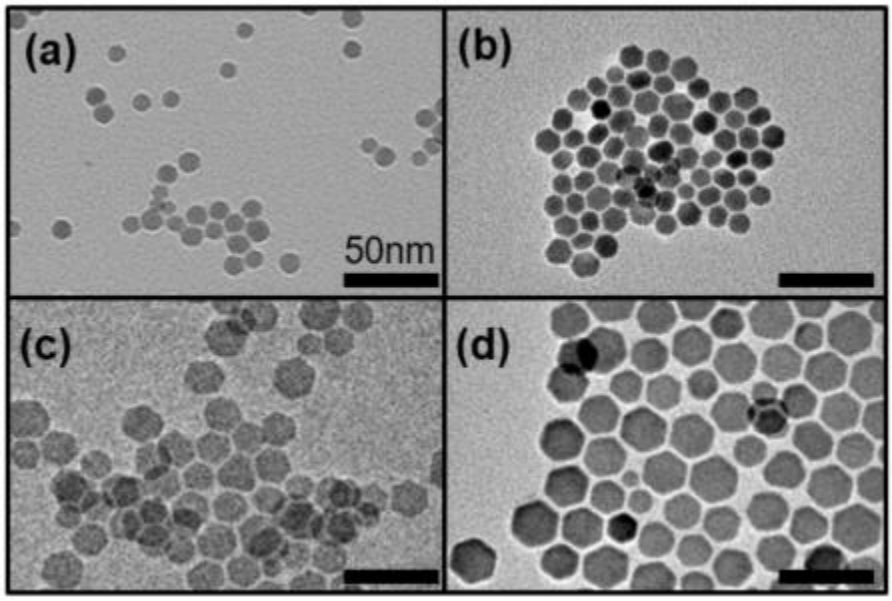

Figure. 13 Transmission electron microscope (TEM) images of NPs synthesized using high concentration method, and the size is varied by changing the sulfur content. The particle sizes are (a) 9.9 nm ± 12.0%, (b) 12.5 nm ± 10.0%, (c) 18.0 nm ± 15.3%, and (d) 26.9 nm ± 24.7%

$Cu_{1.81}S$ roxbyite nano-disks were synthesized through our method of decomposition of organometallic precursors at concentrations high enough to control the size and prevent Ostwald ripening [5]. This high concentration method is a one-pot, heat-up process that enables these products to scale to large quantities, and is highly reproducible [5]. To control the size, we varied the precursor ratio Cu:S from 2 : 1.00 to 2 : 1.55, achieving a size series from 9.9 nm to 26.9 nm with size dispersion ranging from 10.0% to 24.7% (**Fig. 12**) (XRD is shown in SI **Fig. 24**). All of the sample sets (all four sizes of particles) have a hexagonal morphology with only a small variation in the thickness (nanodisk side view TEM image shown

in SI **Fig. 23**) the smallest diameter particles are Based on ***Table. 5,*** the thinnest and the thickness increases as diameter increases. Hence, we have a controlled set of particles with similar particle morphology and thickness while isolating a single parameter: the lateral size of the nano-disks.

Table. 5 Diameter and Thickness Comparison Between the Four Sets of roxbyite Nanodisks

Diameter (nm)	9.9	12.5	18.0	26.9
Diameter increases	Reference	26.3%	81.8%	171.7%
Thickness (nm)	5.5	5.9	6.6	6.9
Thickness increases	Reference	7.3%	20.0%	25.5%

The $Cu_{1.81}S$ nano-disks are processed into electrodes using standard methods. Briefly, after washing the nano-disks with dimethyl carbonate to remove the unreacted precursors and excess ligands, the active material is mixed with carbon black and polyvinylidene fluoride (PVDF), both 10% by weight. Electrodes are then made using a doctor blade (10 microns thickness) onto a porous carbon current collector and cut into 1 cm diameter disks. The disks are loaded into coin cells with LiTFSi dissolved in 1,3-dioxolane/1,2-dimethylether as an electrolyte, polytetrafluoroethylene (PTFE) membrane as the separator, and Li metal as the anode (Experimental details are shown in SI).

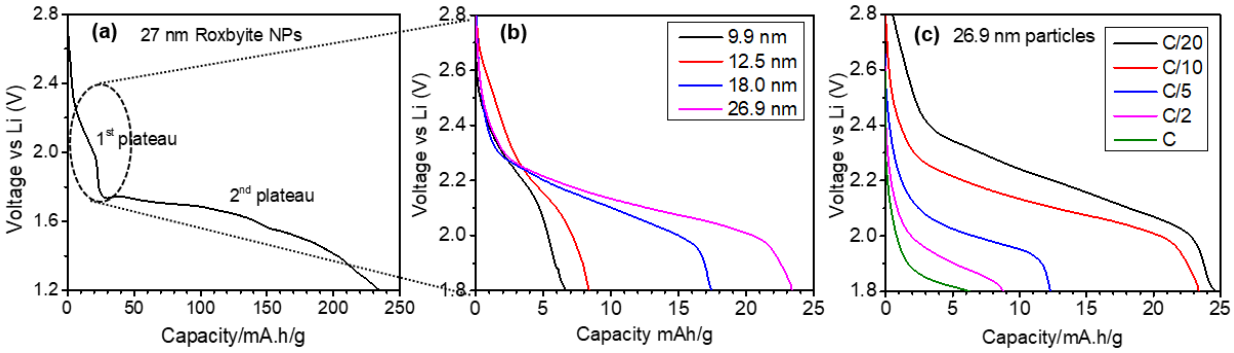

Figure. 14 Electrochemical performance of roxbyite phase NPs. (a) Discharge curve at C/10 rate in the voltage range of 2.7 V to 1.2 V showing plateaus at ~2 V and ~1.6 V. (b) Discharge curves at C/10 rate for four different sizes roxbyite phase NPs showing size dependent plateau lengths. (c) Discharge curves for 26.9 nm roxbyite NPs at different cycling rates.

Galvanostatic charge-discharge (GCPL) studies on the samples show two plateaus in the discharge curve when cycled between 1.2 V to 2.7 V at C/10 rate (the 26.9 nm sample shown in ***Fig. 13*, other sizes are shown in SI Fig. 25**). The two plateaus are separated by the sharp change in gradient at around 1.8 V. The first plateau is observed between 2.7 V to 1.8 V, and the second plateau between 1.8 V and 1.2 V. According to the literature [2], the theoretical capacity of the $Cu_{2-x}S$ are between 340 mA.h/g (Cu_2S) and 560 mA.h/g (CuS). As for $Cu_{1.81}S$, the theoretical capacity is calculated to be 363 mA.h/g (calculation shown in SI). Previous reports [1], [88] state the Cu_2S first cycle discharge capacity is between 250 to 300 mA.h/g (1.4V - 2.4V voltage window), and the capacity quickly decreases to less than 50% within ten cycles. Because roxbyite has a stoichiometry close to Cu_2S, the first cycle discharge capacity (235 mA.h/g) we obtained from our 26.9 nm roxbyite particle is in good agreement with the reported value. Also, the capacity rapidly decreases to less than 50% within three cycles. (shown in SI **Fig. 26**)

Although the mechanism of the second plateau (1.8 V to 1.2 V) has been well understood as displacement reaction [66], [68], [65], the first plateau (2.7 V to 1.8 V) has received relatively little attention. Moreover, that is the focus of this paper. To study the first plateau, GCPL experiments are conducted in the voltage range of 2.7 V to 1.8 V for all nano-disks (***Fig. 13(b)***). As the particle size decreases, the length of the discharge plateau decreases. To understand the rate dependence of the first plateau

reaction we discharged the 26.9 nm roxbyite particles at different discharge rates, from 1 hour to 20 hours (***Fig. 13(c)***). As the discharge rate decreases from C/1 to C/20, the plateau length gradually increases and the specific capacity increases. Moreover, between C/10 and C/20, there is only a 5% capacity increase, indicating that at C/20 the reaction is near equilibrium. The discharge rate and size dependent capacity are summarized in ***Table. 6***. Hence, we mainly focus on the thermodynamic reasons behind the size-dependence for the first plateau.

Table. 6 Discharge rates dependent (26.9nm) and size dependent capacity summary

Discharge rate	1C	C/2	C/5	C/10	C/20
Capacity (mA.h/g)	6.0	8.6	12.2	23.2	24.6
Size (nm)	9.9	12.5	18.0	26.9	
Capacity (mA.h/g)	6.6	8.2	17.4	23.3	

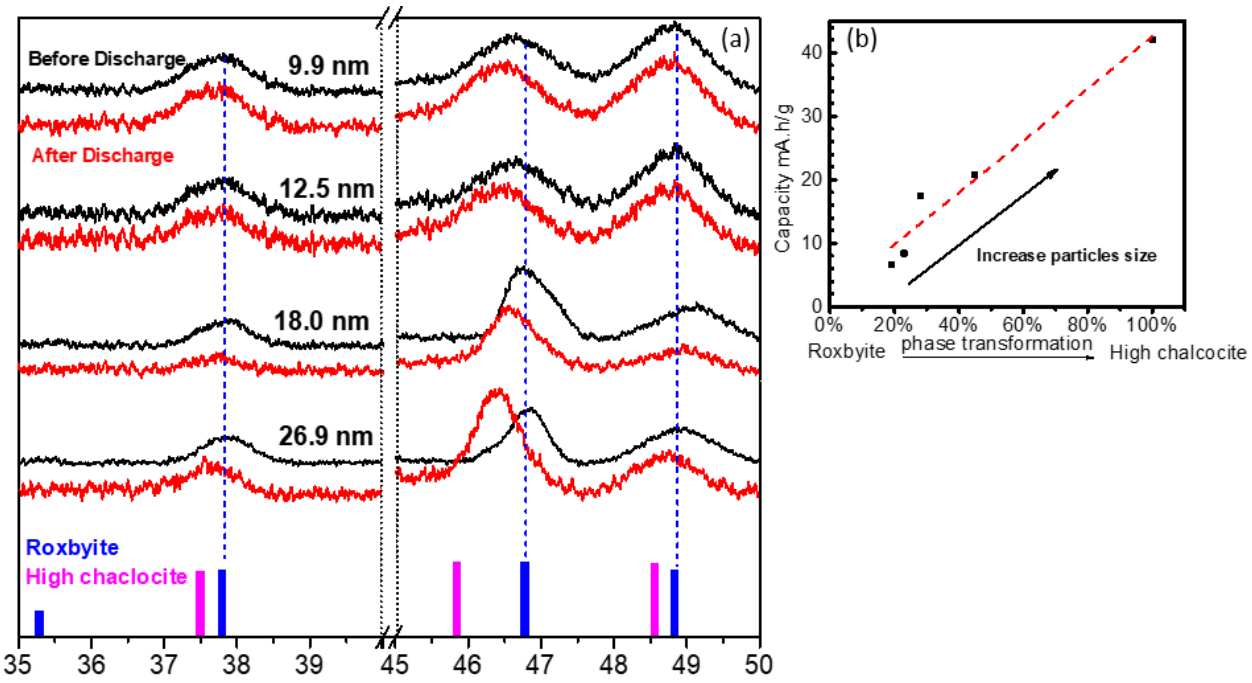

Figure. 15 (a) Ex-situ XRD plots: four different sizes roxbyite nano-disks (9.9 nm to 26.9 nm) scanned before and after the lithiation. High chalcocite and roxbyite standards provided in the bottom. (b) Specific capacity versus percentage phase transformation between roxbyite and high chalcocite for five different sizes roxbyite particles (9.9 nm, 12.5 nm, 18.0 nm, 26.9 nm, and bulk)

Examination of the structure after the first plateau shows a size-dependent peak shifting toward lower two-theta which indicated a phase transformation. *Ex-situ* X-ray diffraction (XRD) of the electrode samples (roxbyite nano-disks and coated carbon) is taken before (2.8V, shown in black) and after (1.8 V, shown in red) discharge (***Fig. 14a***, full range data in **SI *Fig.27***). Before the discharge, all four samples' phases have a good agreement with the roxbyite standard. After the discharge, the XRD patterns show differences from the before-discharge patterns. The main differences are found in the 37.8°, 46.5° and 48.8° peaks. For all four sizes, the three characteristic peaks shifted toward lower two-theta values after lithiation. Additionally, the peaks shift increases as particle size increases ***Table. 7***.

Table. 7 Peak shifts after the discharge comparing with roxbyite standard, the last column shows the difference between roxbyite and high chalcocite standard

Peak shift compares with roxbyite standard (degree)	37.8° peak	46.8° peak	48.8° peak
9.9 nm	0.10	0.19	0.06
12.5 nm	0.08	0.23	0.07
18.0 nm	0.18	0.28	0.15
26.9 nm	0.18	0.45	0.15
High Chalcocite for reference	0.35	1.0	0.35

Based on the data in **Table. 7**, after the discharge, all three characteristic peaks of the initial roxbyite phase shifted toward lower two theta which indicates either a lattice expansion or phase transformation toward high chalcocite phase.

Table. 8 Full-width half max (FWHM) of the 46.5 degree peak before and after the discharge for all four sizes

	9.9nm	12.5nm	18.0nm	26.9nm
Before discharge	1.13	0.91	0.64	0.48

After discharge	1.13	0.93	0.72	0.7
Percentage change	0.0%	2.2%	12.5%	45.8%

To differentiate lattice expansion from phase transformation, the full-width half maxes (FWHM) of the 46.5° are measured for all four sizes using a Gaussian fitting. (**Table. 8)** The FWHM increases after the discharge. Also, the percentage increase in FWHM is larger for larger size particle (2.2% for 12.5 nm and 45.8% for the 26.9 nm particle). The size-dependent FWHM increase suggests the peak shifting observed in ***Fig. 14*** is due to phase transformation since the 45.8% increase in FWHM for 26.9nm particles is more likely to be caused by the superposition of roxbyite and high chalcocite peak as compared to lattice expansion. Hence, the reaction mechanism for all four sizes particle is proposed to be the reaction below

$$1.1\ Cu_{1.81}S + 0.1\ Li \rightarrow Cu_2S + 0.05\ Li_2S$$

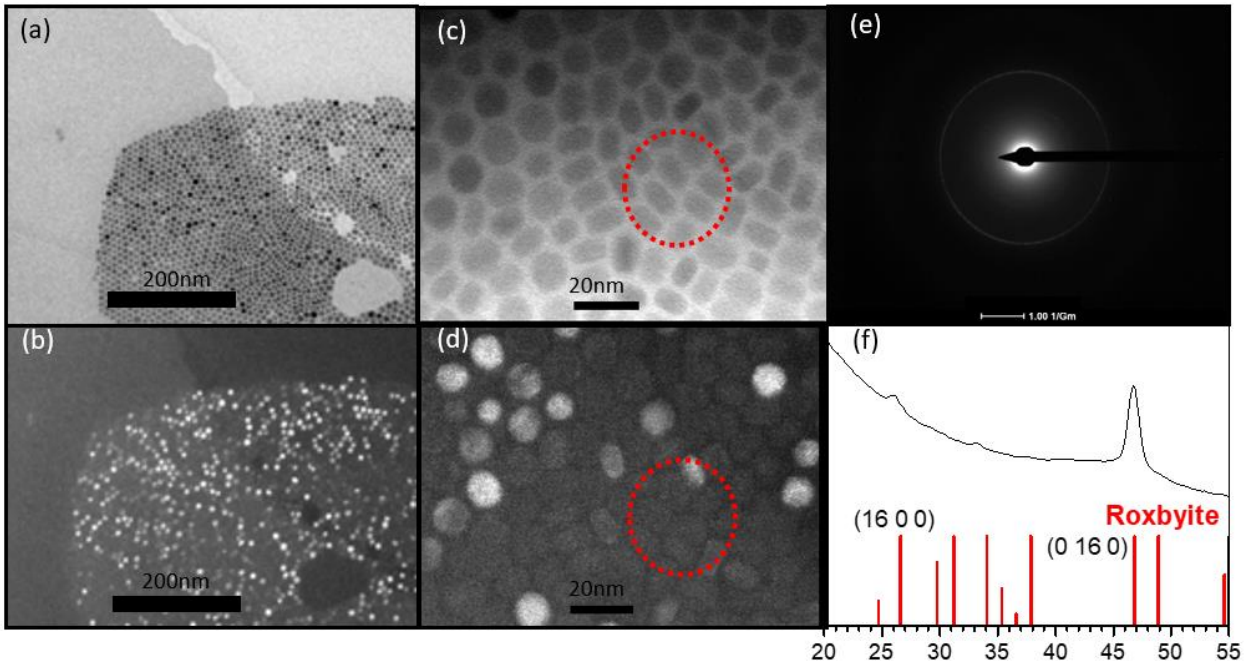

*Figure. 16 (a) Bright field image of selected diffraction regions showing 12.5 nm roxbyite phase NPs.**(**b) Corresponding dark field image. (c) Zoomed-in view of the region with both edge-on and flat particles. (d) Corresponding dark field image with only the flat particles diffracting. (e) Electron diffraction pattern and (f) Integrated pattern (calibrated using a standard aluminum sample).*

To index the nanodisks, the transmission electron microscope (TEM) dark-field experiment is conducted on 12.5 nm roxbyite nano-disks. In ***Fig. 15 a and b***, the selected area for electron diffraction is shown in both bright field and dark-field imaging modes respectively. In ***Fig. 15b***, only part of the disk lights up in the dark- field experiment. To facilitate a better understanding of the particle morphology, higher magnification bright field and dark-field images are shown in ***Fig. 15c and 15d***. In ***Fig. 14c,*** the majority of the particles have the axial direction of the disk facing the beam. However, some particles have its radial direction facing the beam (circled in red). In ***Fig. 15d***, only the only the axial plane lights up in the dark field, which means the diffraction ring we have selected during the dark-field experiment corresponds to the plane normal to the axial direction. Furthermore, in ***Fig. 15e***, only one obvious diffraction ring is observed. Using an aluminum standard for calibration, an integrated electron diffraction pattern is calculated and shown in ***Fig. 15f*****.** Overall, one major peak and two minor peaks are observed. After calibrating with the standard, two peaks are indexed. The strong peak at 46.8 ^{o} corresponds to (0 16 0), and the 26.5 ^{o} peak corresponds to (16 0 0). Based on the data provided above, the plane normal to the axial direction is (0 16 0), and the plane normal to the radial direction is (16 0 0). The indexing result is shown in ***Fig. 16*****.** Additionally, several other researchers arrived at the same index conclusion for hexagonal roxbyite nanodisk [89]**,** [13]**.**

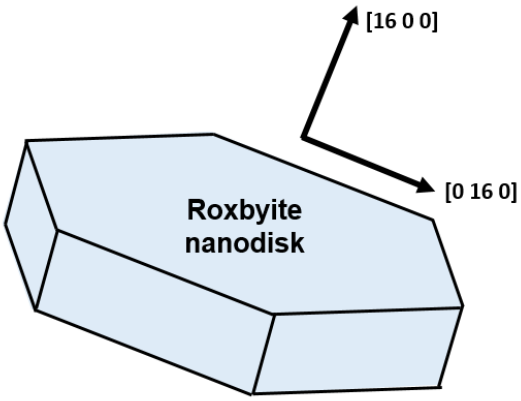

Figure.17 Schematic for the roxbyite nano-disk with indexing

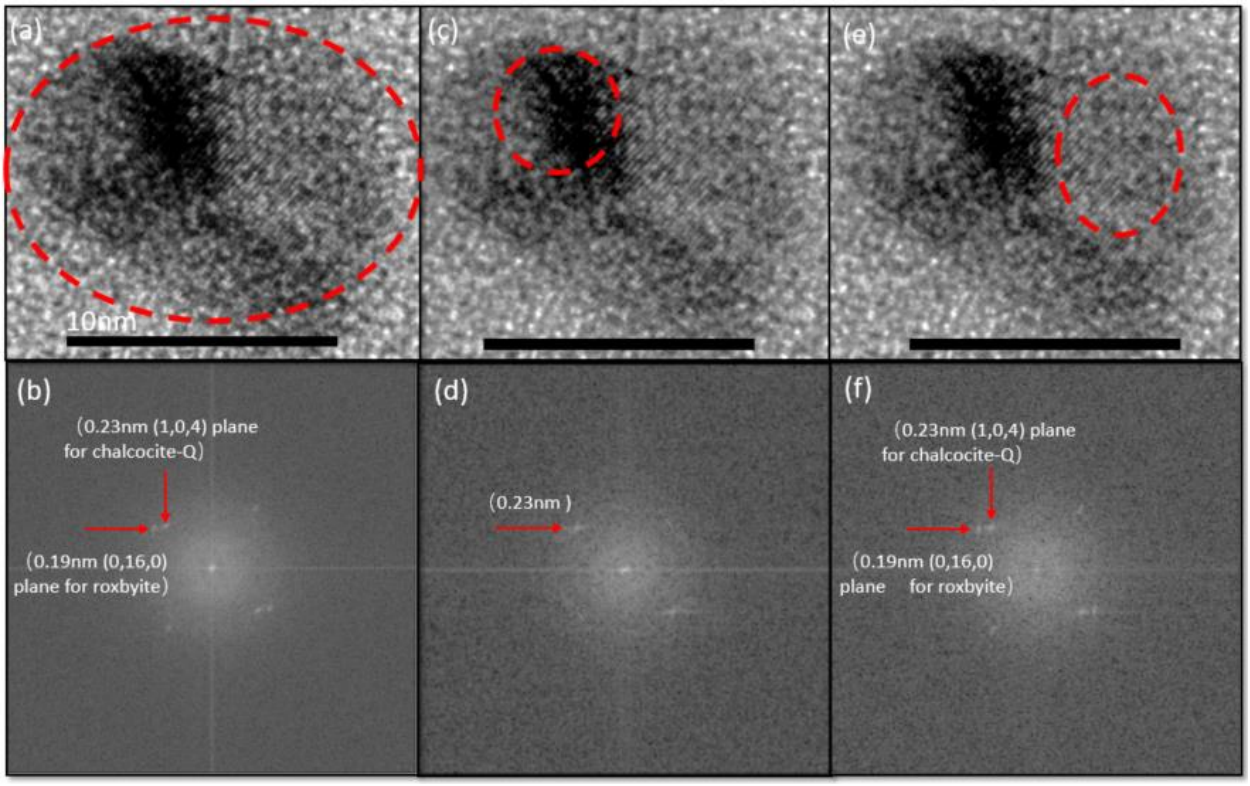

Figure. 18 (a) HRTEM image of the particle (b) Corresponding Fast Fourier transform (FFT) of the entire particle. (c) HRTEM image is highlighting the darker colored area. (d) Corresponding FFT image. (e) HRTEM is highlighting the lighter colored area. (f) Corresponding FFT image. (All the scale bars are 10 nm)

To study the reaction mechanism for the first plateau, *ex-situ* high-resolution transmission electron microscope (HRTEM) experiment is conducted on 26.9 nm roxbyite particle after discharge through the first plateau. After lithiation, the 26.9nm particle breaks into several small pieces. (shown in ***Fig. 30***), One of the pieces is selected and shown in ***Fig. 17***. The HRTEM images are shown in ***Fig. 17a, c, e***. The particle of interest shows irregular shape after reaction with lithium. Additionally, the particle shows a very strong atomic contrast between the left and right regions (shown in red circle in ***Fig. 17c and e***. ***Fig. 17b, d, f*** shows the results of the Fast Fourier Transform (FFT) for the corresponding circled areas are shown. In ***Fig. 17b***, two sets of lattice d-spacings are found. 0.19 nm corresponds to (0 16 0) plane for roxbyite phase, and 0.23 nm corresponds to (1 0 2) plane for high chalcocite phase. (fitting standards in **SI** ***Fig. 11***) In ***Fig. 17b*****,** the relatively darker part of the particle is circled, and the FFT results show only one set of d-spacing which is equal to 0.23 nm. However, in ***Fig. 17f***, two sets of d-spacings are observed with a decrease in clarity compared to ***Fig. 17b.*** The HRTEM results suggest that after reacting with lithium ion, the initially uniform hexagonal roxbyite particle goes through morphology change and phase segregation. Furthermore, the HRTEM data suggest that Li is reacting from the side of the nano-disk since reaction from the axial plane will result in a more uniform particle. Interestingly, similar preferential intercalation behavior was observed for CuS as well [90]. Also, the observed high chalcocite is consistent with the phase transformation mechanism proposed.

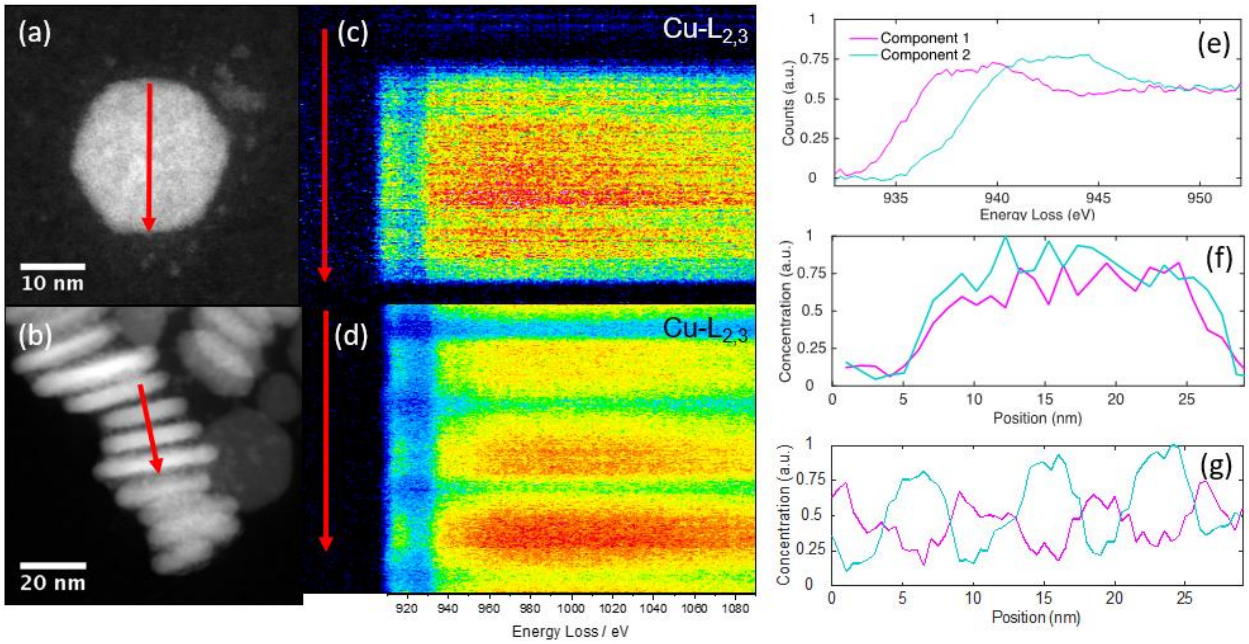

Figure.19 EELS scan of 18.0nm in roxbyite particle. (a) Line scan along ab plane (flat particle) (b) line scan through the c axis (3 stacked particles) (c) EELS energy spectrum for scanning flat disk (x-axis represent 910eV to 1090eV) (d) EELS energy spectrum for scanning stacked disks, (x-axis is 910eV to 1090eV) (e) Multivariate Curve Resolution (MCR) of the EELS spectrum. (f) Concentration profiles of the two resolved spectrums along the ab plane (g) Concentration profiles of the two resolved spectrum along the stacked particles

To understand what causes the size-dependent electrochemical property, electron energy loss spectroscopy (EELS) is conducted for 18.0nm in diameter particle. The results are shown in Figure 18. The nanoparticles are scanned through the ab plane and the c axis separately. (Fig. 18(a), Fig. 18(b)). The corresponding energy spectrums on the right show for the ab plane, the energy is relatively uniform. However, along with the c axis, an obvious energy oscillation is shown as we scan across three disks. Using Multivariate Curve Resolution (MCR), the recorded Cu-L3 edge energy is separated into two components (**Fig.18 (e)**). Using the two components, energy spectrums along c-axis and ab plane are fitted (**Fig.18 (f) (g)**). The fitted results show the component 1 and 2 are relatively uniform when scanning across ab plane. However, along the c axis, the component 1 dominate on the edge of the disk and component 2 take over in the core of the disk. The eels results show that the energy loss is higher in the core of the disk compared to the edge of the disk. The energy oscillation is not directly observable in fig .18 (c), (d) is due to the energy difference between the two components is relatively small compared

to the energy scale on the x-axis. **Fig. 18 (d)** is reproduced (In SI **Fig. 30**) with the smaller x-axis (925 eV to 950 eV) for direct observation of the energy oscillation.

The EELS results have profound implication for the size-dependent electrochemical property. According to the literature [86], for the $LiCoO_2$ particle, the size-dependent plateau length is explained by a lattice gas model simulation based on the fact that the chemical potential for on the edge of the particle is different from the core. Using EELS, they found the Co-L3 edge energy is reduced along the particle edge. Although, when scanning through the ab plane, there is no obvious variation. We observed very similar behavior on Cu-L3 edge. As such, the same theory can be used to explain the size-dependent electrochemical properties we observed.

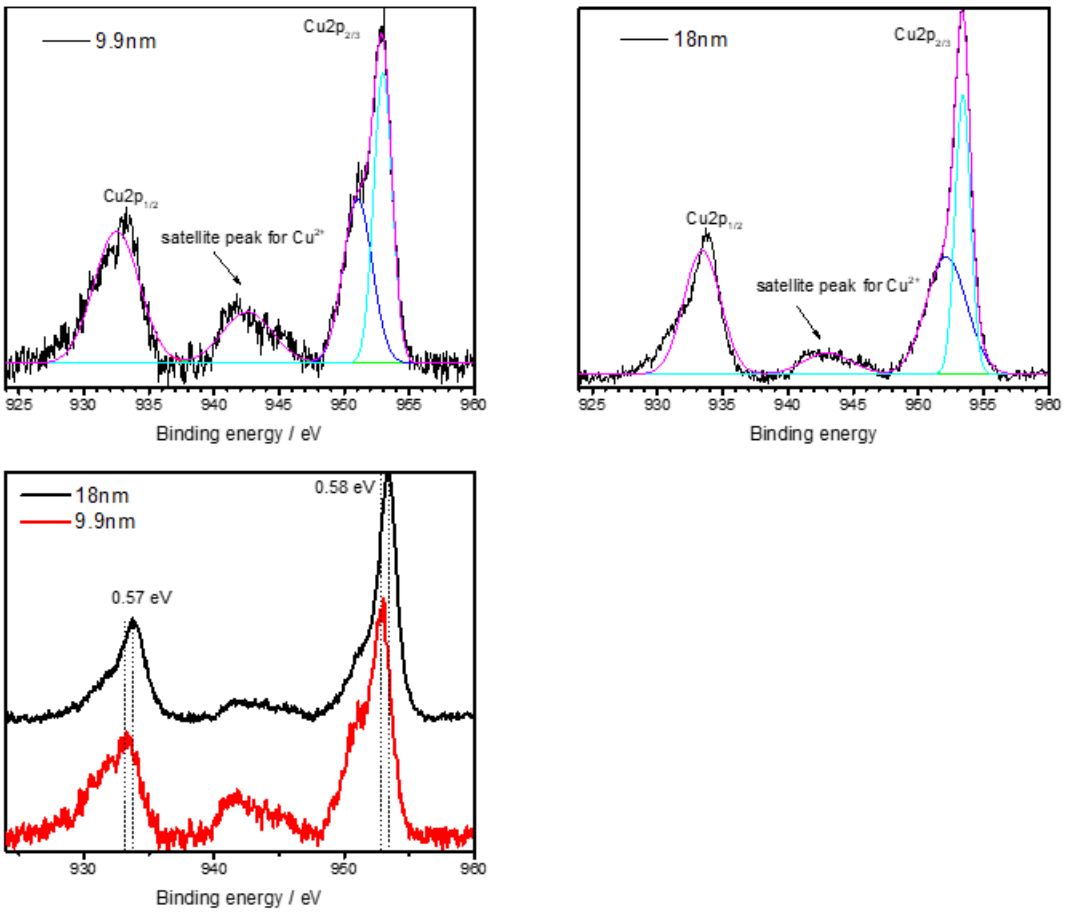

Figure.20 X-ray photoelectron spectroscopy(XPS) results for 9.9nm and 18.0nm roxbyite nanodisks

To explain the energy oscillation observed in the EELS spectrum, XPS was conducted to study the oxidization state of copper. Based on **Fig.19**, both 18.0 nm and 9.9 nm particles have peaks at 953 eV (Cu 2p 1/2) and 933eV (Cu 2p 2/3). Although, the spectrum for the 9.9 nm particle is shifted toward left for about 0.58 eV. Also, between 945 eV to 938 eV, a broad satellite peak was observed for both samples. Although, in comparison, in 9.9 nm roxbyite sample, this satellite peak is much more pronounced compared to the 18.0 nm roxbyite sample.

According to the literature [91], [92], the satellite peaks around 940 eV to 945 eV and the shifting of the 931 eV peak are known to indicate the presence of Cu^{2+} ion. Based on the XPS spectrum present above, 9.9 nm roxbyite particles have significantly more Cu^{2+} present compared to the 18.0 nm. The oxidization state difference between different size particles explains the energy oscillation we observed in EELS as nonuniform oxidization state throughout the particle. The presence of Cu^{2+} is most likely to be caused by surface oxidization. Since small particle has a higher surface to volume ratio, it has more Cu^{2+} present in the XPS spectrum. More importantly, this could explain the size-dependent electrochemical properties we observed since large particle has a smaller fraction of Cu^{2+} ion present.

Future work

Strictly air free experiments as a control to prove the proposed theory

In our experiment, we concluded the surface oxidization leads to the size-dependent electrochemical properties. To confirm this conclusion, we can do the same experiments with the completely air free condition. If the size dependence disappears, that means our theory is correct. If there is still a size dependence, we need to explore the other reasons to explain the size dependence.

Better ligand removal method

Ligand attaching to the particle is inevitable from the colloidal synthesis which leaves to poor conductivity. The current ligand removal method is either annealing at 250 degree Celsius which leads to

particle growth or treated with ammonium sulfide which leads to elemental S attaching to the particle surface. A better ligand removal method is required which preserves the original particle morphology and leaves no excess material on the particle.

Better chemical potential profile for more sound discharge curve modeling

A more accurate discharge curve modeling requires more accurate chemical potential profile throughout the particle. A 3D EELS mapping and an ab into simulation should be conducted simultaneously for better accuracy.

Conclusion

We have shown that by using different sizes roxbyite ($Cu_{1.81}S$) nanodisks (9.9 nm-26.9 nm), there is a size-dependent plateau (2.1 V) when discharged versus Li. Using high-resolution TEM, we managed to study individual nanoparticle during the lithiation process and found Li-ion are preferentially reaction through the side of the hexagonal nanodisks ((0 16 0) plane). Moreover, based on the result from the electron energy loss spectroscopy and X-ray photoelectron spectroscopy, the size-dependent electrochemical property is explained by the different oxidization ratio between Cu^{2+} and Cu^{1+}. The smaller particle has a higher amount of Cu^{2+} present which leads to the size-dependent electrochemical curve.

Supporting Information

Particle Size Measurement

To measure the size and size dispersity of the particle, at least one hundred of particles from each sample is manually measured by Image J line profile. Moreover, the average size and standard deviation are calculated using data acquired.

Theoretical Capacity Calculation

The chemical formula is $Cu_{1.81}S$

C (theoretical max capacity) = $\frac{x_{mx} \cdot F}{3.6 MW_{\mathrm{host}}}$

Where x_{mx} = maximum amount of Li ions per unit host

F = e*Na = 96485 C/mol (Faraday)

MW_{host} = host molecular weight.

3.6 just converts to mAh/g

C (theoretical max capacity) = $\frac{x_{mx} \cdot F}{3.6 MW_{\mathrm{host}}}$=363.6 mAh/g

Modeling the Discharge Capacity

V: volume of the material

E: Li Intercalation voltage

r: distance from the center of the particle to the edge of the particle

r_0: radius of the particle

C: the capacity of the material

t: thickness of the disk

Based on literature [85], [93], we did a simple model of the discharge curve based on the size of the particle.

The Li intercalation/extraction voltage V is determined by the lithium chemical potential difference between the cathode and anode (also called lithium site energy) [94].

$$V = -\frac{u_{Li}^{cathode} - u_{Li}^{anode}}{zF}$$

Based on our EELS data, we found the site energy is higher on the surface compared to the core. The energy difference was previously observed in $LiCoO_2$ nanoparticle in which the top 3 nm for LiCoO2 [86]. In our model we assume on the surface, the chemical potential is -1.2 eV versus Li, in the core, it is -2.1 eV, and the chemical potential linearly decreases through the top 4.5nm of the material.

First, we made some assumption about the geometry and Li intercalation voltage. Based on the data from EELS, we know the electronic structure of the surface 4-5 nm is different from the core. So we assumed the top 4.5nm of the particle has different $u_{Li}^{cathode}$ compare to the core. Also, the particle is assumed to be spherical to simplify the calculation.

Moreover, we assumed a linear potential drop with the distance which is shown below *fig. 21*

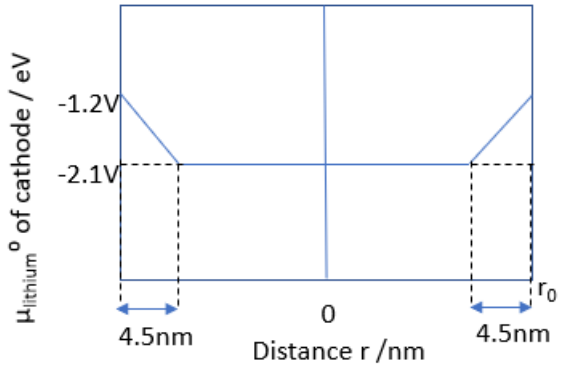

Figure. 21 Li intercalation voltage as a function of the particle dimension.

Based on the potential profile, the intercalation voltage from the center of the particle to the edge can be described by the figure below.

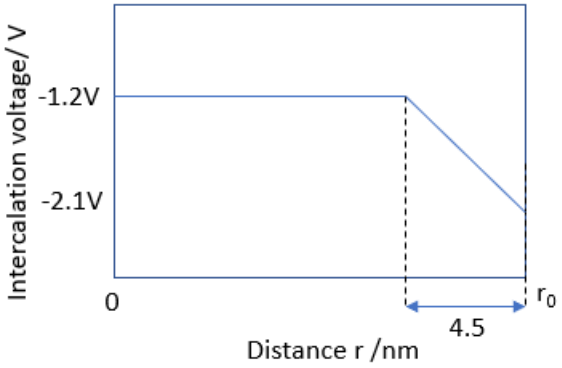

Figure.22 Li intercalation voltage as a function of distance to the center of the particle

Mathematically it can be described by the equations below

$$E = 2.1 \qquad (r < (r_0\text{-}4.5))$$

$$E = 1.2 - 0.2(r - r_0) \qquad ((r_0\text{-}4.5) \leq r \leq r_0)$$

The next step is finding a relationship between the Volume of material V and the capacity C. Since the volume of material reacted can determine the specific capacity we get

$$\mathrm{C} = \mathrm{kV}$$

Also, C to V has the relationship below, and can find the constant k by combining the two equations

$C_{core} = C_{total} * V_{core}/V_{total}$ $k = C_{total}/V_{total}$

(Note: C_{core} means the Capacity in the area with $r < r_0 - 4.5$)

The third step is finding a relationship between the volume of material V and the distance to the core r.

$$dV = 2\pi r dr * t$$

C_{total} is calculated by letting the material going through the reaction below, and it is 42 mAh/g

$$Cu_{1.81}S + 2\ Li^+ = Li_2S + 0.905\ Cu_2S$$

Now we have three relationships:

V – r $dC = \frac{C_{total}}{V_{total}} \mathrm{dV}$.....1

V – C $dV = 2\pi r dr * t$.....2

E - r $E = 1.2 - 0.2(r - r_0)$ $(r >= (r_0\text{-}4.5))$

Using the three equation, we can solve a relationship between Capacity and radius of the particle r_0. The solution is shown below

$E(C) = \frac{r_0+6}{5} + \frac{\sqrt{C{r_0}^2 - {r_0}^2 x + 42{r_0}^2 + 504 r_0 + 1512}}{5\sqrt{42}}$ in which C is $C_{total}(1 + \frac{36+12r_0}{{r_0}^2})$

Substituting in all four particle sizes 9.9nm, 12.5nm, 18.0nm, and 27.0nm, we can obtain a discharge curve for all of them which is shown below *Fig.22*.

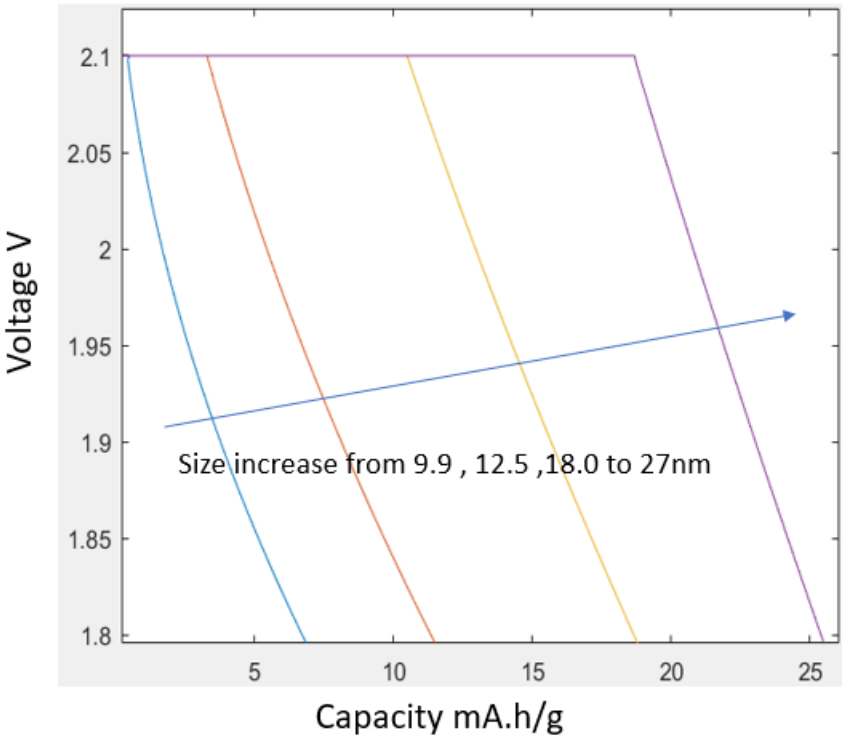

Figure. 23 Simulation discharge curve for four different sizes particle between 2.1 to 1.8V. Blue (9.9nm), Orange (12.5nm), Yellow (18.0nm) and Purple (27.0nm)

The simulated capacity is compared with the actual capacity we obtained from experiment and is shown in **Fig.28.**

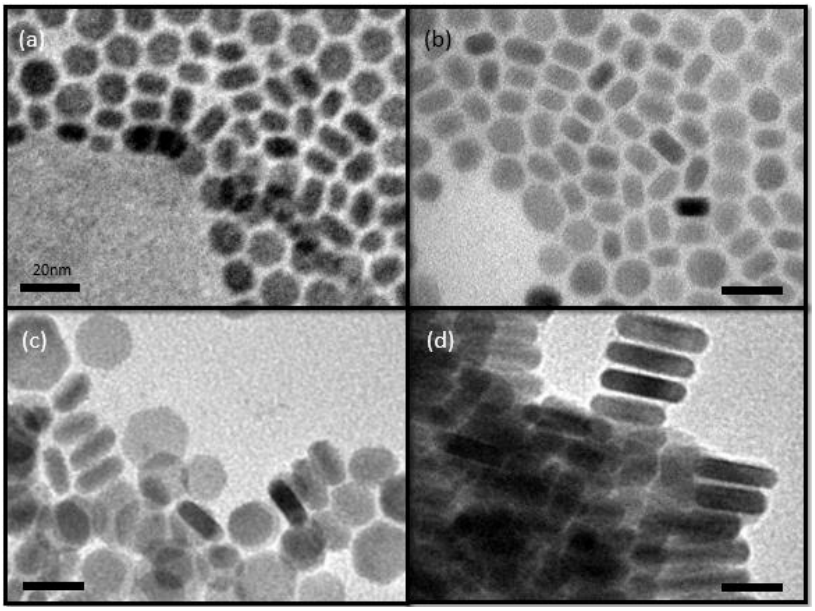

Figure. 24 Four different size particles imaged from the side. (a) 9.9 nm in diameter, 5.5 nm in thickness (b) 12.5 nm in diameter, 5.9 nm in thickness (c) 18.0 nm in diameter, 6.6 nm in thickness (d) 26.9 nm in diameter, 6.9 nm in thickness

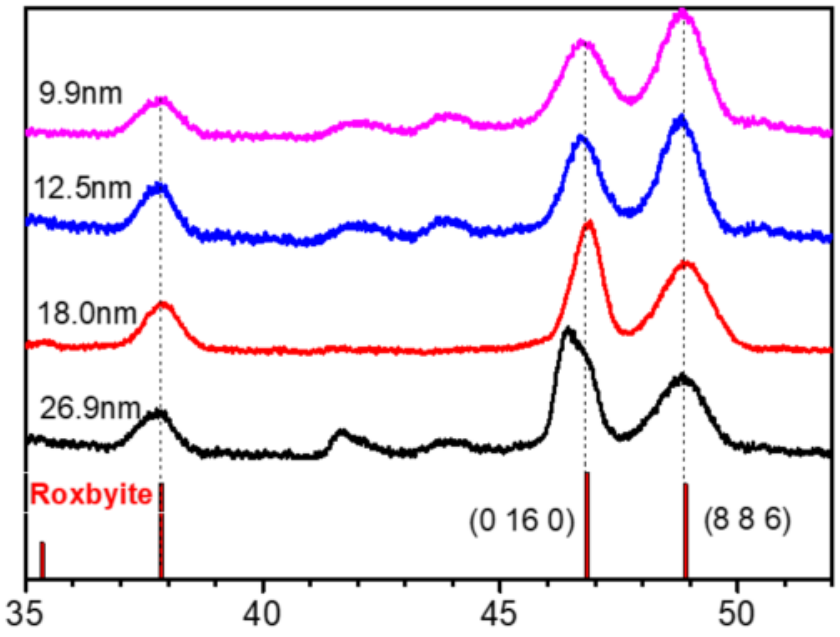

Figure. 25 X-ray diffraction for four different size particles

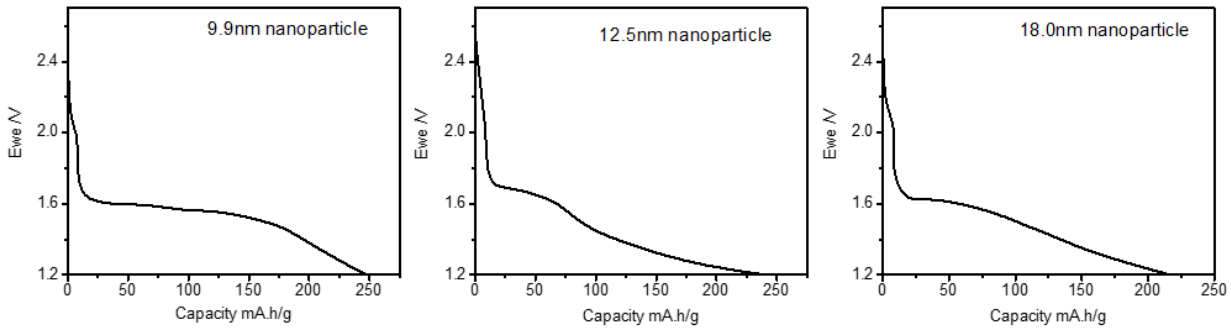

Figure. 26 Discharge curve at C/10 rate in the voltage range of 2.7 V to 1.2 V for 9.9 nm,12.5 nm, 18 nm roxbyite nanoparticles

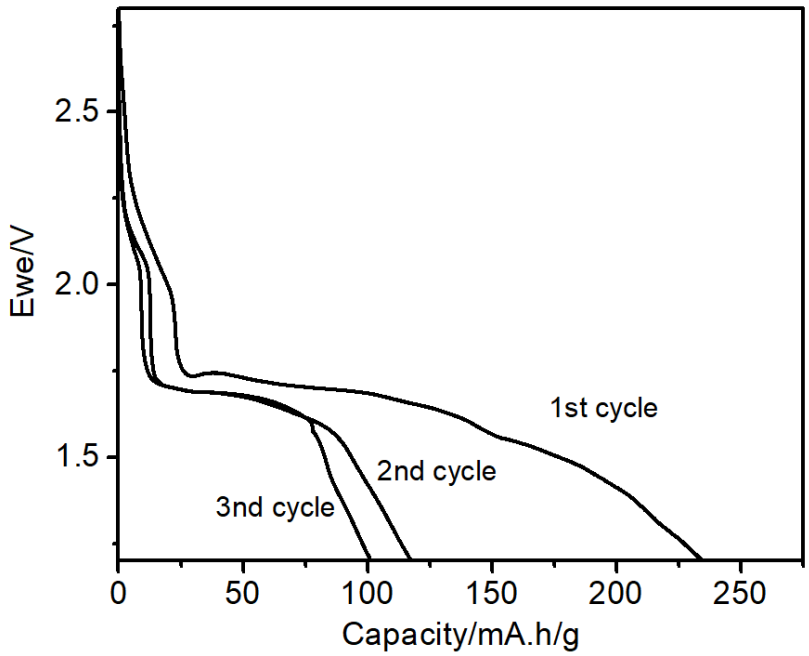

Figure. 27 27nm roxbyite first three discharge cycles. Capacities rapidly decrease.

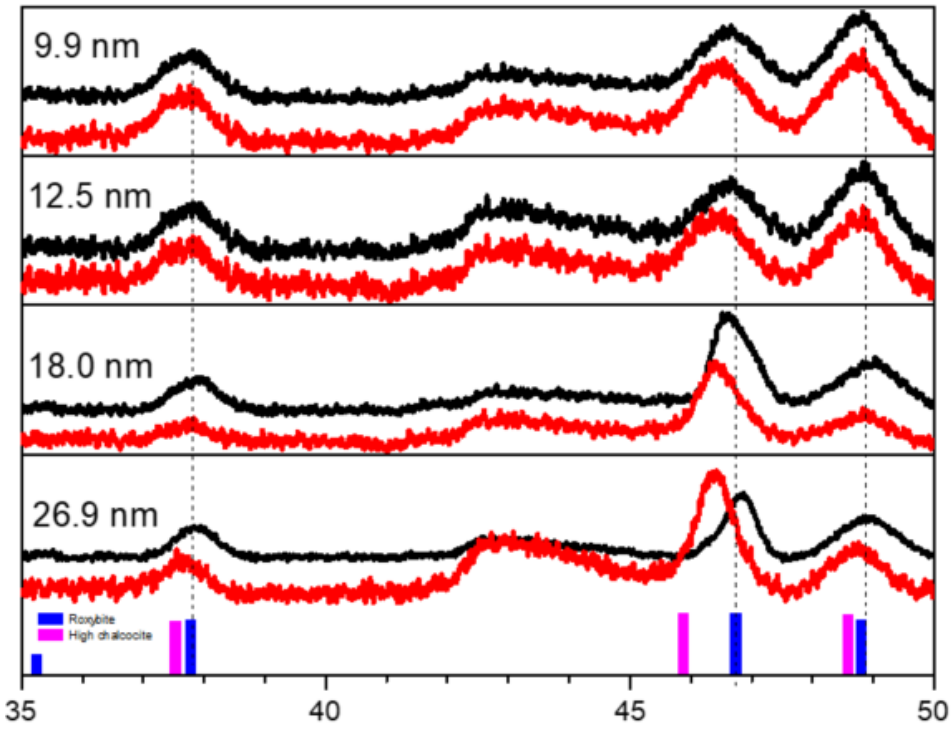

Figure. 28 Ex-situ XRD full range data for four different sizes

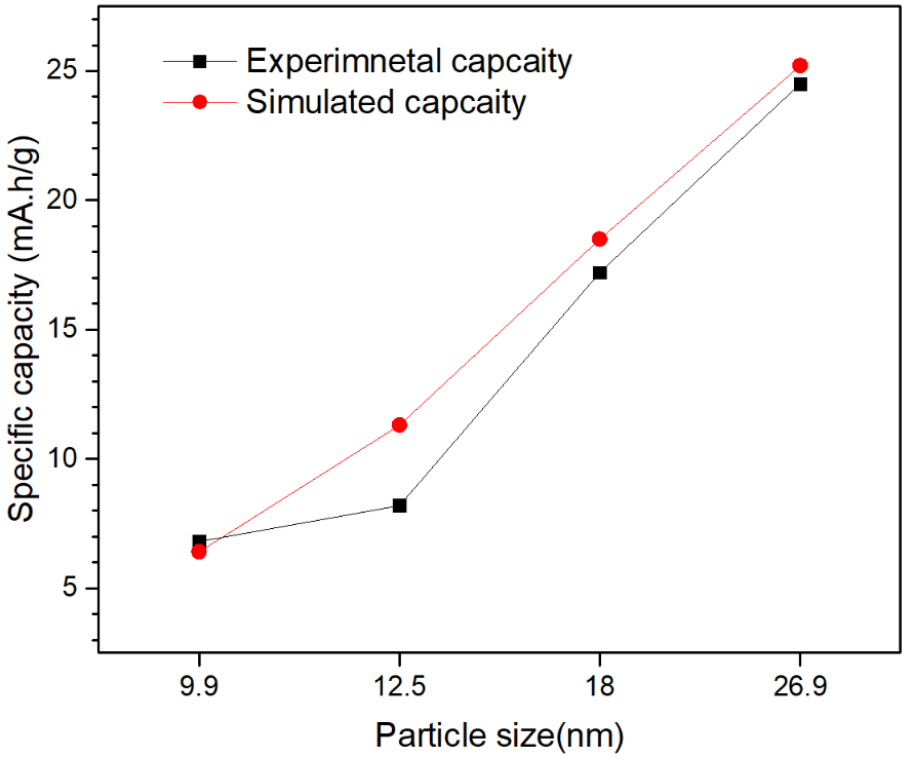

Figure. 29 Experimentally obtained capacities versus simulated capacity for four different sizes

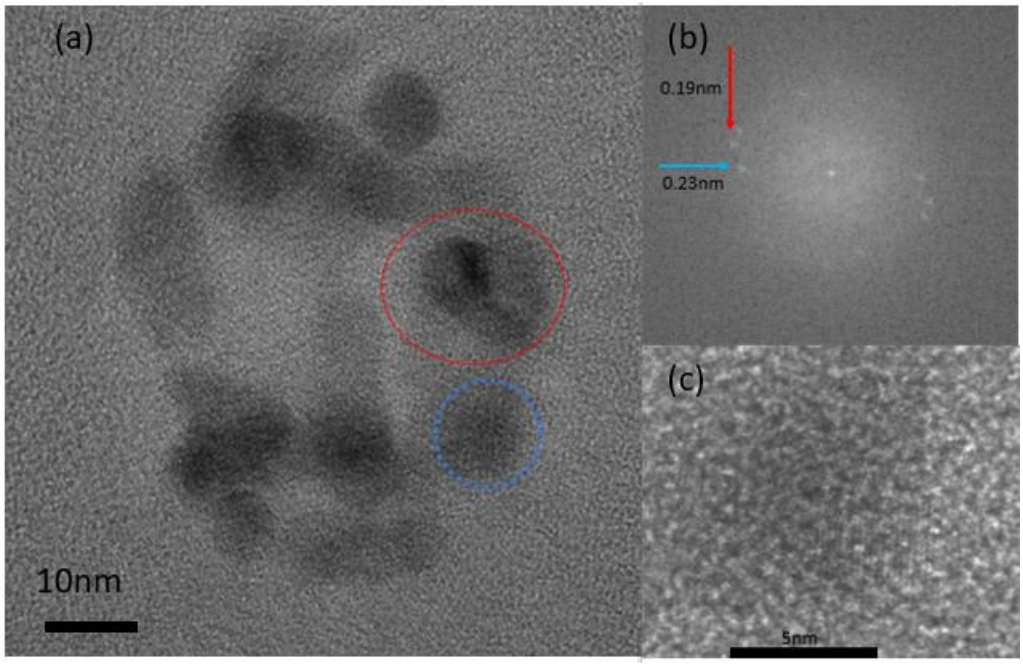

Figure. 30 High-resolution TEM (a) Whole particle after lithiation (inside the red dash circle is the particle analyzed in the paper,). (b) Fast Fourier transform of the particle shown in (c). (c) The particle selected for fast Fourier transformation.

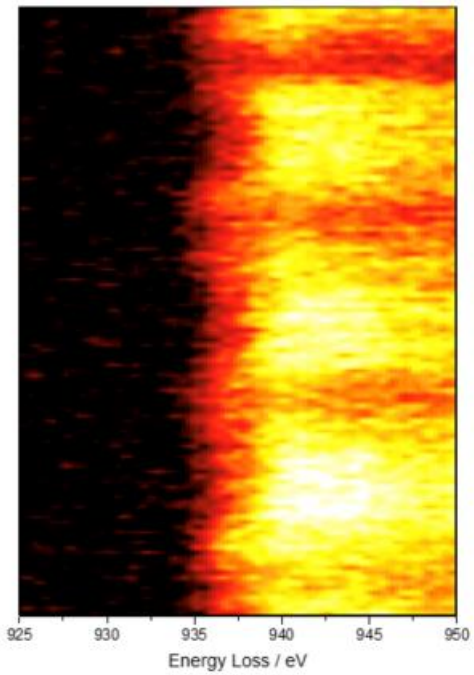

Figure. 31 Reproduced Fig.19 (d) with a smaller x-axis (925 eV to 950 eV) for direct observation of the energy oscillation effect.

Chapter 3: Future work

In-situ TEM during first discharge plateau

All the TEM images we acquired in this study is based on *ex-situ* study. The *ex-situ* TEM data provide us with information about the reaction process and the end product. However, there are some questions cannot be solved by *ex-situ* TEM experiment. For example, we cannot tell whether the chalcocite and roxbyite phase segregation is due to the phase segregation after the reaction or caused by directional lithiation process. *In-situ* TEM experiment provides us opportunities to directly observe the reaction process.

Kinetically Limited versus Thermodynamically Limited Discharge

During the experiment, the discharge rate was kept under C/10 which means a the lithiation process is under thermodynamically stable condition. However, fast discharge is feasible for $Cu_{2-x}S$ due to the high ionic mobility. It will be interesting to study whether the first plateau reaction mechanism varies depending on the discharge rate.

Prevent Oxidization of the $Cu_{2-x}S$ Particle

As we understand from our size-dependent electrochemical study, the size-dependence is closely related to the oxidization state difference between the surface and core of the particle. However, whether the oxidization state difference is caused by oxidization in the air or it is intrinsic to the particle and formed during synthesis is still unknown. As such, I am planning to study the oxidization

state difference between different size particles in air free condition throughout the particle synthesis and XPS sample preparation (in the glove box).

Ligand Removal

The ligand is imperative for nanoparticle colloidal synthesis since it prevents particle aggregation and growth. However, surface ligand leads to very high resistance. The current method of ligand removal is either heating the particle to 230 °C or ligand exchange using ammonium sulfide. The first method leads to particle growth and the second one lead to element S accumulate on top of the particle. A more reliable way of removing the ligand is required.

Carbon - Copper Sulfide core shell structure

The size-dependent study provides us with some insight into why $Cu_{2-x}S$ nanoparticle sometime does not reach theoretical capacity during the discharge. If we can mitigate the surface oxidization problem, then we might be able to reach the same discharge capacity as we reduce the size of the particle. One method has been proposed. Using the salt matrix templating method, it is possible to carbonize the surface ligand through high-temperature annealing without causing particle aggregation. Salt matrix templating will form a core-shell nanoparticle with a protective and conductive carbon shell with an active $Cu_{2-x}S$ core. The exact way of making the core-shell nanoparticle still need to be investigated.

Better modeling for the discharge curve

A better potential profile throughout the particle is required for better discharge curve modeling. The potential profile can be obtained either through ab into calculation or more sophisticated EELS measurement.

Bibliography

[1] E. al. F. Bonino, M. Lazzari, “Electrochemical Behaviour of Solid Cathode Materials in Organic Electrolyte Lithium Batteries: Copper Sulfides,” *J.electrochem.Soc*, vol. 131, no. 7, pp. 1498–1502, 1984.

[2] B. J. Cabana, L. Monconduit, D. Larcher, and M. R. P. Palacín, “Beyond Intercalation-Based Li-Ion Batteries : The State of the Art and Challenges of Electrode Materials Reacting Through Conversion Reactions,” *Adv. Energy Mater. views*, vol. 22, no. 35, pp. 170–192, 2010.

[3] S. K. Kimihiko Okamoto, “Electrical Conduction and Phase Transition of Copper Sulfides,” *Jpn. J. Appl. Phys.*, vol. 12, no. 8, pp. 1130–1138, 1973.

[4] A. Etienne, “Electrochemical Methods to Measure the Copper Ionic Diffusivity in a Copper Sulfide Scale,” *J.electrochem.Soc*, vol. 117, no. 7, pp. 870–874, 1971.

[5] C. B. Williamson, D. R. Nevers, T. Hanrath, and R. D. Robinson, “Prodigious Effects of Concentration Intensification on Nanoparticle Synthesis: A High-Quality, Scalable Approach.,” *J. Am. Chem. Soc.*, vol. 137, no. 50, pp. 15843–51, Dec. 2015.

[6] M. J. B. Bernhardt J. Wuensch, “The crystal structure of Chalcocite, Cu2S,” *Mineral. Soc. Am. Spec. Pap. 1*, pp. 164–170, 1963.

[7] D. E. T. Chakrabarti, D. J.; Laughlin, “The Cu-S (Copper-Sulfur) System. Bull. Alloy Phase Diagrams,” *Bull. Alloy Phase Diagrams*, vol. 4, p. 254, 1983.

[8] H. T. Evans, “The crystal structures of low chalcocite and djurleite *,” *Zeitschrift Fur Krist.*, vol. 150, pp. 299–320, 1979.

[9] Q. Xu, B. Huang, Y. Zhao, Y. Yan, R. Noufi, S. Wei, Q. Xu, B. Huang, Y. Zhao, Y. Yan, R. Noufi, and S. Wei, “Crystal and electronic structures of Cu x S solar cell absorbers,” *Appl. Phys. Lett.*, vol. 100, p. 061906–(1–4), 2012.

[10] Y. Zhang, Y. Wang, L. Xi, and R. Qiu, “Electronic structure of antifluorite Cu2X (X = S , Se , Te) within the modified Becke- Johnson potential plus an on-site Coulomb U,” *J. Chem. Phys.*, vol. 120, p. 120, 2014.

[11] L. Nail, “Djurleite (Cu1.94S) and low Chalcocite CU2S new Crystal Structure studies,” *Science (80-.).*, vol. 203, pp. 356–358, 1979.

[12] S. E. Habas, H. A. S. Platt, M. F. A. M. Van Hest, and D. S. Ginley, “Low-Cost Inorganic Solar Cells : From Ink To Printed Device,” *Chem. Rev.*, vol. 110, pp. 6571–6594, 2010.

[13] H. Zhang, Y. Zhang, J. Yu, and D. Yang, “Phase-Selective Synthesis and Self-Assembly of Monodisperse Copper Sulfide Nanocrystals,” *J. Phys. Chem. C*, vol. 112, pp. 13390–13394, 2008.

[14] W. P. Lim, C. T. Wong, S. L. Ang, and H. Y. Low, “Phase-Selective Synthesis of Copper Sulfide Nanocrystals,” *Chem. Mater.*, vol. 18, pp. 6170–6177, 2006.

[15] D. Zhu, A. Tang, L. Peng, Z. Liu, C. Yang, and F. Teng, “Tuning the plasmonic resonance of Cu2-xS nanocrystals: effect of the crystal phase, morphology and surface ligands,” *J. Mater. Chem. C*, vol. 4, pp. 4880–4888, 2016.

[16] D. Ha, A. H. Caldwell, M. J. Ward, S. Honrao, K. Mathew, R. Hovden, M. K. A. Koker, D. A. Muller,

R. G. Hennig, and R. D. Robinson, “Solid − Solid Phase Transformations Induced through Cation Exchange and Strain in 2D Heterostructured Copper Sul fi de Nanocrystals,” *Nano Lett.*, vol. 14, no. 12, pp. 7090–7099, 2014.

[17] K. K. and N. Morimoto, “The Crystal Structure of Anilite,” *Acta Cryst*, vol. B26, p. 915, 1970.

[18] E. Environ, Y. Zhao, and C. Burda, “Development of plasmonic semiconductor nanomaterials with copper chalcogenide for a future with sustainable energy materials,” *Energy Environ. Sci.*, vol. 5, pp. 5564–5576, 2012.

[19] L. D. Partain, P. S. Mcleod, J. A. Duisman, T. M. Peterson, D. E. Sawyer, C. S. Dean, L. D. Partain, P. S. Mcleod, J. A. Duisman, T. M. Peterson, D. E. Sawyer, and C. S. Dean, “Degradation of a CuxS / CdS solar cell in hot , moist air and recovery in hydrogen and air,” *J. Appl. Phys.*, vol. 54, pp. 6707–6720, 1983.

[20] Y. Zhao, H. Pan, Y. Lou, X. Qiu, J. Zhu, and C. Burda, “Plasmonic Cu 2 - x S Nanocrystals : Optical and Structural Properties of Copper-Deficient Copper (I) Sulfides,” *J. Am. Chem. Soc.*, vol. 131, pp. 4253–4261, 2009.

[21] M. Lot, T. Machani, D. P. Rossi, and K. E. Plass, “Alpha -Chalcocite Nanoparticle Synthesis and Stability,” *Chem. Mater.*, vol. 23, pp. 3032–3038, 2011.

[22] Y. Wu, C. Wadia, W. Ma, B. Sadtler, A. P. Alivisatos, M. Science, V. Di, and L. Berkeley, “Synthesis and Photovoltaic Application of Copper (I) Sulfide Nanocrystals 2008,” *Nano Lett.*, vol. 8, no. 8, pp. 2551–2555, 2008.

[23] A. Nelson, D. Ha, and R. D. Robinson, “Selective Etching of Copper Sulfide Nanoparticles and Heterostructures through Sulfur Abstraction : Phase Transformations and Optical Properties,” *Chem. Mater.*, vol. 28, no. 23, pp. 8530–8541, 2016.

[24] A. H. Caldwell, D. Ha, X. Ding, R. D. Robinson, A. H. Caldwell, D. Ha, X. Ding, and R. D. Robinson, “Analytical modeling of localized surface plasmon resonance in heterostructure copper sulfide nanocrystals Analytical modeling of localized surface plasmon resonance in heterostructure copper sulfide nanocrystals,” *J. Chem. Phys.*, vol. 141, pp. 164125-1–8, 2014.

[25] J. M. Luther, P. K. Jain, T. Ewers, and A. P. Alivisatos, “Localized surface plasmon resonances arising from free carriers in doped quantum dots,” *Nat. Mater.*, vol. 10, no. 5, pp. 361–366, 2011.

[26] B. Elektronenspeicherring and R. Electromagnetique, “Studies of copper valence states with Cu L3 x-ray absorption spectroscopy,” *Phys. Rev. B*, vol. 39, pp. 1541–1545, 1989.

[27] V. A. Online, “Quantitative X-ray absorption and emission spectroscopies : electronic structure elucidation of Cu 2 S,” *J. Mater. Chem. C*, vol. 1, pp. 2448–2454, 2013.

[28] W. L. and M.-H.Whangbo, “Conductivity Anisotropy and structural phase transition in covellite CuS,” *Solid State Commun.*, vol. 85, no. 5, pp. 405–408, 1993.

[29] Y. Xie, A. Riedinger, M. Prato, A. Casu, A. Genovese, P. Guardia, S. Sottini, C. Sangregorio, K. Miszta, S. Ghosh, T. Pellegrino, and L. Manna, “Copper Sul fi de Nanocrystals with Tunable Composition by Reduction of Covellite Nanocrystals with Cu + Ions,” *J. Am. Chem. Soc.*, vol. 135, pp. 17630–17637, 2013.

[30] N. Nitta, F. Wu, J. T. Lee, and G. Yushin, “Li-ion battery materials: present and future,” *Mater.*

Today, vol. 18, no. 5, pp. 252–264, 2015.

[31] Y. Xie, A. Riedinger, M. Prato, A. Casu, A. Genovese, P. Guardia, S. Sottini, C. Sangregorio, K. Miszta, S. Ghosh, T. Pellegrino, and L. Manna, "Copper Sulfide Nanocrystals with Tunable Composition by Reduction of Covellite Nanocrystals with Cu + Ions," *J. Am. Chem. Soc.*, vol. 135, pp. 17630–17637, 2013.

[32] P. K. Presented, "A structural prediction of copper sulfide and study of its electronic properties and vacancy formation trend using density functional theory," *Master Sci. Phys. thesis - Univ. Texas Arlingt.*, no. August, 2014.

[33] P. Lukashev, W. R. L. Lambrecht, T. Kotani, and M. Van Schilfgaarde, "Electronic and crystal structure of Cu2 − xS : Full-potential electronic structure calculations," *Phys. Rev. B*, no. 76, pp. 1–14, 2007.

[34] C. Coughlan, M. Ibáñez, O. Dobrozhan, A. Singh, A. Cabot, and K. M. Ryan, "Compound copper chalcogenide nanocrystals," *Chem. Rev.*, vol. 117, no. 9, pp. 5865–6109, 2017.

[35] and J. Y. Weimin Du, Xuefeng Qian, Xiaodong Ma, Qiang Gong, Hongliang, Cao, "Shape-Controlled Synthesis and Self-Assembly of Hexagonal Covellite (CuS) Nanoplatelets," pp. 3241–3247, 2007.

[36] L. Liu, H. Zhong, Z. Bai, T. Zhang, W. Fu, L. Shi, H. Xie, L. Deng, and B. Zou, "Controllable Transformation from Rhombohedral Cu 1.8 S Nanocrystals to Hexagonal CuS Clusters: Phase- and Composition- Dependent Plasmonic Properties," *Chem. Mater.*, vol. 25, pp. 4828–4834, 2013.

[37] Y. Xie, L. Carbone, C. Nobile, V. Grillo, S. D. Agostino, F. Della Sala, C. Giannini, D. Altamura, C. Oelsner, X. C. Kryschi, P. D. Cozzoli, V. Arnesano, I.- Lecce, L. Carbone, V. G. Moruzzi, and I.- Pisa, "Metallic-like Stoichiometric Copper Surface Plasmon Resonance Properties , and Their Modeling," *ACS Nano*, vol. 7, no. 8, pp. 7352–7369, 2013.

[38] Q. Lu, F. Gao, and D. Zhao, "One-Step Synthesis and Assembly of Copper Sulfide Nanoparticles to Nanowires , Nanotubes , and Nanovesicles by a Simple Organic Amine-Assisted Hydrothermal Process," *Nano Lett.*, vol. 2, no. 7, pp. 725–728, 2002.

[39] J. Zou, J. Zhang, B. Zhang, P. Zhao, and K. Huang, "Low-temperature synthesis of copper sulfide nano-crystals of novel morphologies by hydrothermal process," *Mater. Lett.*, vol. 61, pp. 5029–5032, 2007.

[40] P. Zhang and L. Gao, "Copper sulfide flakes and nanodisks," *J. Mater. Chem.*, vol. 13, pp. 2007–2010, 2003.

[41] X. Li, X. He, C. Shi, B. Liu, Y. Zhang, S. Wu, and Z. Zhu, "Synthesis of One-Dimensional Copper Sulfide Nanorods as High-Performance Anode in Lithium Ion Batteries," *ChemSusChem*, vol. 7, pp. 3328–3333, 2014.

[42] S. Gorai, D. Ganguli, and S. Chaudhuri, "Synthesis of Copper Sulfides of Varying Morphologies and Stoichiometries Controlled by Chelating and Nonchelating Solvents in a Solvothermal Process 2005," *Cryst. Growth Des.*, vol. 5, no. 3, pp. 875–877, 2005.

[43] W. Microemulsions, S. K. Haram, A. R. Mahadeshwar, and S. G. Dixit, "Synthesis and Characterization of Copper Sulfide Nanoparticles in Triton-X 100," *J.Phys.Chem*, vol. 100, pp. 5868–5873, 1996.

[44] J. Kundu and D. Pradhan, “Controlled Synthesis and Catalytic Activity of Copper Sul fi de Nanostructured Assemblies with Di ff erent Morphologies,” *Appl. Mater. interfaces*, vol. 6, pp. 1823–1834, 2014.

[45] T. H. Larsen, M. Sigman, A. Ghezelbash, R. C. Doty, and B. A. Korgel, “Solventless Synthesis of Copper Sulfide Nanorods by Thermolysis of a Single Source Thiolate-Derived Precursor,” *JACS Commun.*, vol. 125, pp. 5638–5639, 2003.

[46] H. Zhang, Y. Zhang, J. Yu, and D. Yang, “Phase-Selective Synthesis and Self-Assembly of Monodisperse Copper Sulfide Nanocrystals,” *J. Phys. Chem.*, vol. 112, pp. 13390–13394, 2008.

[47] Y. Chen, L. Chen, and L. Wu, “The Structure-Controlling Solventless Synthesis and Optical Properties of Uniform Cu 2 S Nanodisks,” *Chem.Eur.J*, vol. 14, pp. 11069–11075, 2008.

[48] L. Chen, Y. Chen, and L. Wu, “Synthesis of Uniform Cu 2 S Nanowires from Copper - Thiolate Polymer Precursors by a Solventless Thermolytic Method,” *J. Am. Chem. Soc. Commun.*, vol. 126, pp. 16334–16335, 2004.

[49] M. B. Sigman, A. Ghezelbash, T. Hanrath, A. E. Saunders, F. Lee, and B. A. Korgel, “Solventless Synthesis of Monodisperse Cu 2 S Nanorods , Nanodisks , and Nanoplatelets,” *J. Am. Chem. Soc.*, vol. 125, pp. 16050–16057, 2003.

[50] A. E. Saunders, A. Ghezelbash, D. Smilgies, M. B. Sigman, and B. A. Korgel, “Columnar Self-Assembly of Colloidal Nanodisks,” *Nano Lett.*, vol. 3, no. 12, pp. 2959–2963, 2006.

[51] X. Du, Z. Yu, and A. Dasari, “Facile Synthesis and Assembly of Cu 2 S Nanodisks to Corncoblike Nanostructures,” *Chem.Mater*, no. 12, pp. 5156–5158, 2006.

[52] J. R. Ahmed Lutfi Abdelhady, Karthik Ramasamy, Mohammad Azad Malik, Paul O’brien, Sarah J.Haigh, “New routes to copper sulfide nanostructures and thin films,” *J. Mater. Chem.*, vol. 21, pp. 17888–17895, 2011.

[53] W. Bryks, M. Wette, N. Velez, S. Hsu, and A. R. Tao, “Supramolecular Precursors for the Synthesis of Anisotropic Cu 2 S Nanocrystals,” *J. Am. Chem. Soc. Commun.*, vol. 136, pp. 6175–6178, 2014.

[54] P. Nørby, S. Johnsen, and B. B. Iversen, “In Situ X - ray Diffraction Study of the Formation, Growth, and Phase Transition of Colloidal Cu 2 À x S Nanocrystals,” *ACS Nano*, vol. 8, no. 5, pp. 4295–4303, 2014.

[55] H. Lee and C. Burda, “Evaluation of the photoinduced electron relaxation dynamics of Cu 1.8 S quantum dots y,” pp. 1091–1095, 2003.

[56] I. J. Plante, T. W. Zeid, and T. Mokari, “Synthesis of metal sulfide nanomaterials via thermal decomposition of single-source precursors †,” no. 20, pp. 6612–6617, 2010.

[57] Z. Liu, D. Xu, J. Liang, J. Shen, S. Zhang, and Y. Qian, “Growth of Cu2S Ultrathin Nanowires in a Binary Surfactant Solvent,” *J.Phys.Chem.B*, no. 109, pp. 10699–10704, 2005.

[58] X. Wang, Y. Ke, H. Pan, K. Ma, Q. Xiao, D. Yin, G. Wu, and M. T. Swihart, “Cu-Deficient Plasmonic Cu2-xS Nanoplate Electrocatalysts for Oxygen Reduction,” *ACS Catal.*, vol. 5, pp. 2534–2540, 2015.

[59] H. Zhang, B. Hyun, F. W. Wise, and R. D. Robinson, “A Generic Method for Rational Scalable Synthesis of Monodisperse Metal Sul fi de Nanocrystals,” *Nano Lett.*, vol. 12, pp. 5856–5860,

2012.

[60] X. Liu, X. Wang, B. Zhou, W. Law, A. N. Cartwright, and M. T. Swihart, “Size-Controlled Synthesis of Cu 2- x E (E = S , Se) Nanocrystals with Strong Tunable Near-Infrared Localized Surface Plasmon Resonance and High Conductivity in Thin Films,” *Mater. views*, vol. 23, pp. 1256–1264, 2013.

[61] C. Wu, S. Yu, and M. Antonietti, “Complex Concaved Cuboctahedrons of Copper Sulfide Crystals with Highly Geometrical Symmetry Created by a Solution Process,” *Chem. Mater2*, vol. 18, pp. 3599–3601, 2006.

[62] V. A. Online, X. Meng, G. Tian, Y. Chen, R. Zhai, J. Zhou, Y. Shi, X. Cao, W. Zhou, and H. Fu, “Hierarchical CuS hollow nanospheres and their structure-enhanced visible light photocatalytic properties,” *CrystEngComm*, vol. 15, pp. 5144–5149, 2013.

[63] Z. Cheng, S. Wang, Q. Wang, and B. Geng, “A facile solution chemical route to self-assembly of CuS ball-flowers and their application as an efficient photocatalyst,” *CrystEngComm*, vol. 12, pp. 144–149, 2010.

[64] B. S. Jiao, L. Xu, K. Jiang, and D. Xu, “Well-Defined Non-spherical Copper Sulfide Mesocages with Single- Crystalline Shells by Shape-Controlled Cu 2 O Crystal Templating **,” *Adv. Mater.*, no. 18, pp. 1174–1177, 2006.

[65] J.-S. Chung and H.-J. Sohn, “Electrochemical behaviors of CuS as a cathode material for lithium secondary batteries,” *J. Power Sources*, vol. 108, pp. 226–231, 2002.

[66] A. Débart, L. Dupont, R. Patrice, and J. Tarascon, “Reactivity of transition metal (Co , Ni , Cu) sulphides versus lithium : The intriguing case of the copper sulphide,” *Solid State Sci.*, vol. 8, pp. 640–651, 2006.

[67] N. Yamakawa, M. Jiang, and C. P. Grey, “Investigation of the Conversion Reaction Mechanisms for Binary Copper (II) Compounds by Solid-State NMR Spectroscopy and X-ray Diffraction,” *Chem. Mater.*, vol. 21, pp. 3162–3176, 2009.

[68] M. T. Mcdowell, Z. Lu, K. J. Koski, J. H. Yu, G. Zheng, and Y. Cui, “In Situ Observation of Divergent Phase Transformations in Individual Sul fi de Nanocrystals,” *Nano Lett.*, vol. 15, pp. 1264–1271, 2015.

[69] J. F. G. and J. V. S. Cassaignon, Th. Pauporte, “Copper Diffusion in Copper Sulfide : a Systematic Study,” *Ionics (Kiel).*, vol. 4, pp. 364–371, 1998.

[70] M. G. Boebinger, M. Xu, X. Ma, H. Chen, R. R. Unocic, and M. T. Mcdowell, “Distinct nanoscale reaction pathways in a sulfide material for sodium and lithium batteries,” *J. Mater. Chem.*, vol. 5, pp. 11701–11709, 2016.

[71] J. Schuster, G. He, B. Mandlmeier, T. Yim, K. T. Lee, T. Bein, and L. F. Nazar, “Spherical Ordered Mesoporous Carbon Nanoparticles with High Porosity for Lithium – Sulfur Batteries ** Angewandte,” *Angew. Chemie*, vol. 51, pp. 3591–3595, 2012.

[72] M. Nagarathinam, K. Saravanan, W. L. Leong, P. Balaya, and J. J. Vittal, “Hollow Nanospheres and Flowers of CuS from Self-Assembled Cu (II) Coordination Polymer and Hydrogen-Bonded Complexes of N - (2-Hydroxybenzyl) - L -serine,” 2009.

[73] S. Yang, Xiuchun; Lu, Wei; Hou, Junwei; Li, Xiaoning; Han, "Room-Temperature Synthesis of High-Density CuS Nanowire Arrays by a Simple Paired Cell," *J. Nanosci. Nanotechnology,* vol. 11, no. 11, pp. 9818–9822, 2011.

[74] L.-J. C. Chen-Ho Lai, Kuo-Wei Huang, Ju-Hsiang Cheng, Chung-Ynag Lee, Bing-Joe Hwang, "Direct growth of high-rate capability and high capacity copper sulfide nanowire array cathodes for lithium-ion batteries," *J. Mater. Chem.*, vol. 20, pp. 6638–6645, 2010.

[75] Y. Du, Z. Yin, J. Zhu, X. Huang, X. Wu, Z. Zeng, Q. Yan, and H. Zhang, "A general method for the large-scale synthesis of uniform ultrathin metal sulphide nanocrystals," *Nat. Commun.*, vol. 3, p. 1177, 2012.

[76] C. K. Chan, H. Peng, G. Liu, K. McIlwrath, X. F. Zhang, R. A. Huggins, and Y. Cui, "High-performance lithium battery anodes using silicon nanowires," *Nat. Nanotechnol.*, vol. 3, no. 1, pp. 31–35, 2008.

[77] T. Journal, M. C. Weeks, E. Voss, S. Yoshizawa, S. Okada, R. T. Mathieson, P. Press, E. L. Jones, G. Papazov, D. Pavlov, T. M. Company, E. J. Ritchie, and C. Manufacturing, "All-Solid Lithium Electrodes with Mixed-Conductor Matrix," *J.Electrochem. SocElectrochemical Sci. Technol.*, vol. 128, no. 4, pp. 725–728, 1981.

[78] Y. Liu, N. S. Hudak, D. L. Huber, S. J. Limmer, J. P. Sullivan, and J. Y. Huang, "In situ transmission electron microscopy observation of pulverization of aluminum nanowires and evolution of the thin surface Al2O3 layers during lithiation-delithiation cycles," *Nano Lett.*, vol. 11, no. 10, pp. 4188–4194, 2011.

[79] X. H. Liu, L. Zhong, S. Huang, S. X. Mao, T. Zhu, and J. Y. Huang, "Size-dependent fracture of silicon nanoparticles during lithiation," *ACS Nano*, vol. 6, no. 2, pp. 1522–1531, 2012.

[80] L. D. & J.-M. T. P.poizot, S. Laruelle, S. Grugeon, "ChemInform Abstract : Nano-Sized Transition-Metal Oxides as Negative-Electrode Materials for Lithium-Ion Batteries . Nano-sizedtransition-metaloxidesas," *Nature*, vol. 407, pp. 496–499, 2000.

[81] S. Paek, E. Yoo, and I. Honma, "Enhanced Cyclic Performance and Lithium Storage Capacity of SnO 2 / Graphene Nanoporous Electrodes with," *Nano Lett.*, vol. 9, pp. 72–75, 2009.

[82] M. Ge, J. Rong, X. Fang, and C. Zhou, "Porous Doped Silicon Nanowires for Lithium Ion Battery Anode with Long Cycle Life," *Nano Lett.*, vol. 12, pp. 2318–2323, 2012.

[83] D. Wang, D. Choi, J. Li, Z. Yang, Z. Nie, R. Kou, C. Wang, L. V Saraf, J. Zhang, I. A. Aksay, J. Liu, D. Wang, D. Choi, J. Li, Z. Yang, Z. Nie, R. Kou, and D. Hu, "Roxbyite, a New Copper Sulphide Mineral from the Olympic Dam Deposit, Roxby Downs, South Australia," *ACS Nano*, vol. 3, pp. 907–913, 2009.

[84] V. Augustyn, P. Simon, and B. Dunn, "Pseudocapacitive oxide materials for high-rate electrochemical energy storage," *Energy Environ. Sci.*, vol. 7, no. 5, p. 1597, 2014.

[85] M. Okubo, E. Hosono, J. Kim, M. Enomoto, N. Kojima, T. Kudo, H. Zhou, and I. Honma, "Nanosize effect on high-rate Li-ion intercalation in LiCoO2 electrode," *J. Am. Chem. Soc.*, vol. 129, no. 23, pp. 7444–7452, 2007.

[86] M. Okubo, J. Kim, T. Kudo, H. Zhou, and I. Honma, "Anisotropic Surface Effect on Electronic Structures and Electrochemical Properties of," *J.Phys.Chem. C*, vol. 113, pp. 15337–15342, 2009.

[87] H.-S. Kim, J. B. Cook, S. H. Tolbert, and B. Dunn, “The Development of Pseudocapacitive Properties in Nanosized-MoO2,” *J. Electrochem. Soc.*, vol. 162, no. 5, pp. A5083–A5090, 2015.

[88] Y. Fu and A. Manthiram, “Electrochemical properties of Cu2S with ether- based electrolyte in Li-ion batteries,” *Electrochim. Acta*, vol. 109, pp. 716–719, 2013.

[89] D. Y. H. Seungyeol Lee, Seungmin Baek, Joong Pill Park, Ju Hyun Park and and S.-W. K. Sang Kyu Kwak, “Transformation from Cu2−xS Nanodisks to Cu2−xS@CuInS2 Heteronanodisks via Cation Exchange,” *Chem. Mater.*, vol. 28, pp. 3337–3344, 2016.

[90] K. He, Z. Yao, S. Hwang, N. Li, K. Sun, H. Gan, Y. Du, H. Zhang, C. Wolverton, and D. Su, “Kinetically-Driven Phase Transformation during Lithiation in Copper Sul fi de Nano fl akes,” *Nano Lett.*, vol. 17, pp. 5726–5733, 2017.

[91] M. C. Biesinger, L. W. M. Lau, A. R. Gerson, R. St, and C. Smart, “Applied Surface Science Resolving surface chemical states in XPS analysis of first row transition metals , oxides and hydroxides : Sc , Ti , V , Cu and Zn,” *Appl. Surf. Sci.*, vol. 257, no. 3, pp. 887–898, 2010.

[92] M. C. Biesinger, B. R. Hart, R. Polack, B. A. Kobe, and R. S. C. Smart, “Analysis of mineral surface chemistry in flotation separation using imaging XPS,” *Miner. Eng.*, vol. 20, pp. 152–162, 2007.

[93] M. Okubo, E. Hosono, J. Kim, M. Enomoto, N. Kojima, T. Kudo, H. Zhou, and I. Honma, “Nanosize Effect on High-Rate Li-Ion Intercalation in LiCoO 2 Electrode,” *J. Am. Chem. Soc.*, vol. 129, pp. 7444–7452, 2007.

[94] A. Urban, D. Seo, and G. Ceder, “Computational understanding of Li-ion batteries This article has been corrected since publication and a corrigendum has also been published,” *npj Comput. Mater.*, 2016.